Thin-Walled Structures 186 (2023) 110704

Contents lists available at ScienceDirect

Thin-Walled Structures

journal homepage: www.elsevier.com/locate/tws

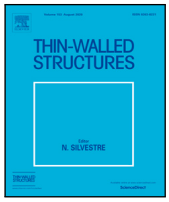

Full length article

Experimental investigation of structural behavior of 316L stainless steel and carbon steel slit dampers

BoKyung Hwang, TaeSoo Kim *, YongHan Ahn

Division of Architecture & Architectural Engineering, Hanyang University ERICA, Ansan, Gyeonggi-do, Republic of Korea

ARTICLE INFO

Keywords:
Austenitic stainless steel
Carbon steel
Seismic slit damper
Cyclic loading
Energy dissipation capacity

ABSTRACT

To expand the range of applications for stainless steel in building structures, previous studies have tested the seismic resistance of structural elements and members using a variety of types of stainless steel. Steel slit dampers have been designed and installed for seismic retrofits of building structures. In this study, hysteresis behaviors of austenitic stainless steel (STS316L) and carbon steel (SS275) slit dampers were investigated and compared to demonstrate the excellent seismic performance of stainless-steel slit dampers. Monotonic and cyclic material tests for STS316L and carbon steel were conducted. STS316L had the best seismic performance, with much greater ductility, strength enhancement and cyclic hardening effect than SS275. STS316L with increased nickel (Ni) and reduced chromium (Cr) contents transformed to exhibit twinning induced plasticity (TWIP) steel after yielding under cyclic loading and thus possesses a more stable austenitic microstructure than SS275 and STS304. Loading experiments with STS316L and SS275 slit dampers were performed according to six loading protocols. The fracture shapes, stiffness, ductility, yield strength and energy dissipation capacity also were compared. STS316L dampers provided greater secondary stiffness, ultimate strength, number of cycles and energy dissipation capacity than SS275 dampers. The ultimate strength and normalized energy dissipation capacity of the STS316L specimens were on average 1.53 times and 4.84 times larger, respectively, than those of the SS275 specimens thanks to excellent ductility and strong cyclic hardening effects at the material level. This study proved that the performance of austenitic stainless steel STS316L as a seismic material and slit damper is superior to those of mild carbon steel SS275 and austenitic stainless steel STS304.

1. Introduction

Recent earthquake activity around the world has highlighted the importance of seismic retrofitting of buildings and urban infrastructure, and there is increasing demand for high-performance materials to ensure human life safety. Interest in durable and eco-friendly materials that can help achieve carbon neutrality is also growing. Stainless steel can contribute to solving these problems. Stainless steel can be an attractive alternative to conventional carbon steel due to its high tensile strength, ductility, durability, resistance to fire and corrosion, and aesthetic appearance [1–4]. Many researchers have investigated the application of stainless steel as a reinforcement for structural members at the materials level under monotonic tensile test results. Austenitic stainless steels, which are the most used in the construction field, have a lower yield strength and excellent elongation compared with mild carbon steel, giving them an excellent deformation capacity until fracture. According to the Steel Construction Institute (SCI) design manual for structural stainless steel [5], austenitic stainless steel is chosen for seismic applications because of its deformation capacity before failure. The plastic behavior of stainless steel when subjected to cyclic loading forces, such as those produced by earthquakes, is significantly different from that of conventional carbon steel, making it necessary to demonstrate the seismic performance of stainless-steel materials and structural members. Several studies have been conducted on the hysteretic characteristics of stainless steels under cyclic loading. Nip et al. [6,7] performed low-cycle fatigue tests, examined cyclic axial loading on carbon steel and stainless steel tubular bracing members, and studied the hysteresis response. Zhou et al. [8] conducted experiments and numerical analyses to investigate the performance of austenitic stainless steel tubular members under cyclic axial loading, and proposed a ductility-oriented design approach for stainless steel compressive members. Kim et al. [9] used cyclic loading tests to study the cyclic response of three types of cold-formed square, hollow-section, stainless-steel bracing members and reviewed the stainless-steel design criteria for axial compressive buckling strength. Sarno et al. [10] undertook inelastic static (pushover) and dynamic (response history) analyses of a braced frame system (concentrically braced frames and moment-resisting frames) retrofitted with stainless steel members. The results showed that stainless steel braced frames can improve plastic deformation and offer excellent energy-absorption capacity with

* Corresponding author.
E-mail address: tskim0709@hanyang.ac.kr (T.S. Kim).

https://doi.org/10.1016/j.tws.2023.110704
Received 9 November 2022; Received in revised form 7 March 2023; Accepted 12 March 2023
Available online xxxx

respect to a carbon steel benchmark structure under analysis conditions with the material input of monotonic tensile test results, but not cyclic coupon test results. Steel slit dampers are considered to dissipate seismic energy and mitigate damage to the main structural members of a building through stable hysteretic behavior. Material yielding steel slit dampers are widely used in the seismic reinforcement of new and existing buildings. Most of these dampers have used carbon steel, and many studies have been conducted on strip or slip dampers with various designs [11–15]. Hwang et al. [16] conducted an experiment under cyclic loading on a steel damper using austenitic stainless steel (STS304) and compared the seismic performance with that of an existing carbon steel (SS275) damper. The STS304 damper exhibited lower deformation capacity compared with the carbon steel damper due to brittle behavior caused by transformation-induced plasticity (TRIP) under cyclic loading, and the energy-dissipation capacity was low in a specimen with a large horizontal displacement. Consequently, the total energy dissipation capacity of STS304 damper was 5% lower, on average, than that of the SS275 damper. Nevertheless, the study confirmed that within the specified low-cycle loading protocol and allowable story drift of retrofitted buildings, austenitic stainless steel STS304 slit dampers possessed excellent seismic performance.

However, in order to provide excellent seismic performance during earthquakes and replace carbon steel dampers in terms of the energy absorption capacity, investigation into the hysteretic behavior of slit dampers using austenitic stainless steel that can exhibit sufficient fatigue capacity and ductility even under cyclic loads is needed. The previous study [17] revealed that STS316, an austenitic stainless steel containing molybdenum and increased nickel (Ni) and reduced chromium (Cr) content compared to STS304, exhibits twinning induced plasticity (TWIP), as opposed to TRIP, after material yielding by cyclic loading, thus increasing both ductility and strength at the material level. Therefore, it is necessary to investigate the seismic performance of the steel slit damper made of STS316 as a structural element using the ductility characteristics of stainless steel under low-cycle fatigue loading.

The purpose of this experimental study is to investigate and compare the hysteresis behavior of austenitic stainless steel STS316L, which shows TWIP under cyclic hardening, and carbon steel SS275 in steel slit dampers with aspect ratios that differ from those used in a previous study in order to understand the seismic response of stainless-steel dampers. In addition, this study will provide basic information on the material properties and hysteretic responses of austenitic stainless steel (316 type) slit dampers subjected to cyclic loads for use in parametric finite element analysis, while also helping to calculate the reinforcement effect as seismic devices on structural frames in buildings.

2. Experimental plan and set-up

2.1. General

The microstructural characteristics of austenitic stainless steel used in structural engineering vary depending on the amounts of added chromium (Cr), nickel (Ni), and molybdenum (Mo). The chemical composition and mechanical properties provided by KS D 3705 [18] for austenitic stainless steels STS304 and STS316L are summarized in Table 1, which also includes mild carbon steel SS275 as a general structure (KS D 3503) [19].

STS316 (Type 316 in ASTM [20]) is a modified version of STS304 (Type 304 in ASTM [20]) with the addition of molybdenum, which lends superior resistance to pitting corrosion in chloride environments. STS304L and STS316L are low-carbon and high-nickel versions of STS304 and STS316, respectively. Reducing the carbon content to 0.03% prevents intergranular corrosion and improves machinability and corrosion resistance. This study compares an STS316L damper with an SS275 damper to investigate seismic performance under cyclic loading.

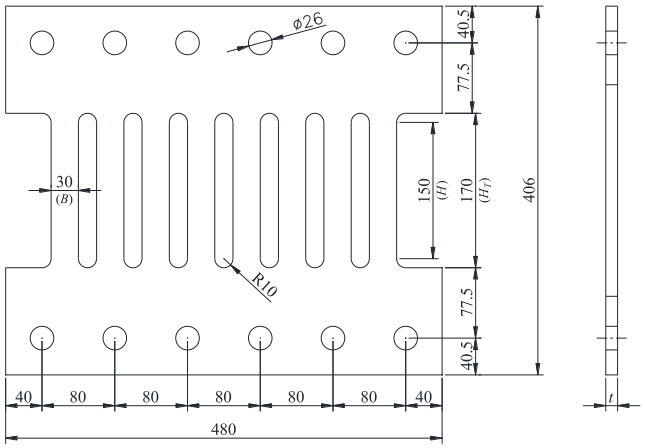

Fig. 1. Detail of specimens (Unit : mm).

2.2. Specimen plan

Slit damper specimens used STS316L (corresponding to ASTM type 316L [20]) with a nominal thickness of 13 mm and SS275 (ASTM A36 [21]) with a nominal thickness of 14 mm. Due to market supply and demand forces for steel, the plate thicknesses of the stainless steel and carbon steel specimens used in this study did not match precisely. Twelve carbon steel SS275 damper (CS2D series) and austenitic stainless steel STS316L damper (SA2D series) specimens were fabricated as listed in Table 2. The main variables of the specimens were steel grade and loading condition. Fig. 1 depicts the shape and dimensions of the specimens. All specimens were 480 mm wide and 406 mm high. The specimens were designed to have an aspect ratio (H/B) of 5.0 with strut width (B) of 30 mm and strut height (H) of 150 mm, excluding the fillet parts of both strut ends. All specimens were composed of eight struts.

Table 2 provides the measured strut thicknesses and strut widths of the specimens, along with loading conditions. There is one monotonic loading protocol, two constant-amplitude cyclic loading protocols, and three incremental-amplitude cyclic loading protocols. “CS2” and “SA2” represent carbon steel (SS275) and austenitic stainless steel (STS316L), respectively, and “D” indicates a steel damper. “M1” denotes monotonic loading, “I” the constant-amplitude cyclic loading protocol, and “G” the incremental-amplitude cyclic loading protocol. Numbers from 1 to 3 are used to differentiate among the loading patterns in a given type of protocol. Details of the loading patterns will be described in Section 2.3.

2.3. Loading protocols

Six types of loading protocols, described in Table 2, were planned: one monotonic load (M1), two constant amplitudes (I2 = 30 mm, I3 = 20 mm), and three incremental amplitudes (G1, G2 and G3). According to the Korean Design Standards (KDS 41) [22], the maximum considered earthquake corresponds to a return period of 2400 years, and the minimum seismic performance target of the building is the level of life safety. At this time, the allowable story drifts of a general non-masonry building are 0.01h for seismic classification S in KDS 41 [22] (risk category IV in ASCE7-16) [23] and 0.015h for seismic classification I in KDS 41 (risk category III in ASCE 7-16), where h is the story height. Therefore, in this study, a building with a floor height of 3.0 m was targeted for seismic retrofit, and the target maximum story drift of the steel slit damper was set at 30 mm. To determine the cyclic loading protocol, the displacement amplitude assumed that the damper was parallel to the structure and resisted the horizontal displacement corresponding to story drift. Fig. 2 depicts the cyclic

Table 1
Chemical composition and material properties limit of damper material in Korea Industrial Standards (KS)

Material	Chemical compositions (%)								Mechanical properties		Common	
	C	Si	Mn	P	S	Ni	Cr	Mo	Yield stress (MPa)	Tensile strength (MPa)	Elongation at fracture (%)	
STS304	≤0.08	≤1.00	≤2.00	≤0.045	≤0.03-	8-10.5	18–20	–	205≤	520≤	40≤	KS D 3705 [20]
STS316L	≤0.03	≤1.00	≤2.00	≤0.045	≤0.03	12–15	16–18	2–3	175≤	480≤	40≤	
SS275	≤0.25	≤0.45	≤1.40	≤0.05	≤0.05	–	–	–	275≤	410–550	18≤	KS D 3503 [21]

* L : Low carbon content.

Table 2
List of specimens.

Specimen	Material	Measured thickness t (mm)	Measured strut width B (mm)	Height of the straight strut part H (mm)	Total height of the strut H_T (mm)	No. struts (EA)	Loading protocol
CS2D-M1	SS275	13.97	30.03	150	170	8	Monotonic
CS2D-I2		13.96	29.89				Constant amplitude −30 mm
CS2D-I3		13.92	29.96				Constant amplitude −20 mm
CS2D-G1		13.98	29.91				FEMA 461
CS2D-G2		13.94	29.92				δ_y based incremental amplitude
CS2D-G3		13.97	29.89				ASCE7-16 (KDS 41 17 00)
SA2D-M1	STS316L	13.17	30.00				Monotonic
SA2D-I2		13.18	29.86				Constant amplitude −30 mm
SA2D-I3		13.21	29.89				Constant amplitude −20 mm
SA2D-G1		13.19	29.97				FEMA 461
SA2D-G2		13.19	29.96				δ_y based incremental amplitude
SA2D-G3		13.20	29.98				ASCE 7-16 (KDS 41 17 00)

loading protocols. To estimate the yield point of the specimen, tests with the monotonic loading protocol (M1) were performed until the lateral force reached the allowable maximum capacity of the actuator; the cyclic tests continued until specimens failed. The steel damper is a displacement-dependent seismic device, and fatigue cracks due to inelastic deformation in the plastic region after damper yielding can shorten the life of the device. To evaluate the damage level of the steel slit damper, cyclic loading with a constant displacement amplitude was applied. The load was applied repeatedly with constant displacement amplitudes of 30 mm (I2) and 20 mm (I3). In addition, the cyclic loading pattern of incremental displacement amplitudes was applied to reflect the accumulated damage, and three loading programs (G1, G2, and G3) were chosen. In loading protocol G1, the load was applied as shown in Fig. 2(b) in accordance with FEMA 461 [24]. The amplitude of each loading step (a_i) in Fig. 2(b) was planned so that the slit dampers had sufficient accumulated plastic deformation experience under cyclic loading. Steps 1 and 2 repeat three cycles each with the lowest amplitude (0.44 mm and 0.62 mm), and from the subsequent step, two cycles are repeated. From Steps 3 to 12, the amplitude (a_i) is applied by increasing the displacement by the same increment (calculated by the equation $a_{i+1} = 1.4a_i$, where a_{i+1} means the amplitude of the next step $i + 1$). After Step 12, the increment is fixed at 5.4 mm and applied until all struts fail [16].

In loading protocol G2, the yield displacement (δ_y) of the specimen obtained by the equation of the steel damper [25,26] and based on the material test results is utilized for the increment of lateral displacement. The lateral displacement was increased up to δ_y, $2\delta_y$, and $4\delta_y$ with three steps for each displacement, and the displacement from the 4th step was repeated twice for each step, increasing the yield displacement by four times as shown in Fig. 2(c). Loading protocol G3 is presented in accordance with ASCE 7-16 criteria [23] and KDS 41 17 00 specifications [22], as can be seen in Fig. 2(d). At the maximum considered earthquake (MCE), the load was applied repeatedly for 10 cycles, 5 cycles, and 3 cycles, at 0.33 times, 0.67 times, and 1.0 times the expected device displacement (Δ_m), respectively. Here, Δ_m was assumed to be 30 mm with allowable story drift (=0.01h, where h is the story height) for a 3 m-story height building, and loading was performed until failure of the steel damper.

2.4. Test set-up

Fig. 3 shows the test set-up for the specimens. One hydraulic actuator with a capacity of 500 kN for cyclic loading was connected to an upper loading beam (BEAM 2), as shown in Fig. 3(a). Lateral supports were installed on both sides of BEAM 2 to prevent lifting and lateral deformation of the rigid beam. Three linear variable displacement transducers (LVDTs) were installed to measure the lateral displacement at each position. LVDT 1 measured the lateral displacement of BEAM 2, while LVDT 2 and LVDT 3 were installed in the direction parallel to the center line of the bolt holes between the T-shaped steel jigs at the top and bottom of each specimen, respectively, to measure the lateral displacement of the strut ends of the steel damper toward the loading direction. The lateral displacement for cyclic loading was controlled by the displacement value of LVDT 2.

2.5. Material mechanical properties under monotonic and cyclic loading

Monotonic tensile coupon and cyclic coupon tests were performed to investigate and compare the material properties of the two steel grades (SS275 and STS316L) used for specimens.

2.5.1. Monotonic tensile coupon tests and results

A monotonic tensile coupon test was performed to investigate the material properties of SS275 and STS316L. Six coupons were cut along the rolling direction with the same plate used to fabricate the specimens, and three were machined for each material according to KS B 0801 [27]. The dimensions for the tensile coupon are illustrated in Fig. 4. The monotonic tensile test was performed in accordance with KS B 0802 [28]. The material test results are summarized in Table 3. Yield stress (F_y) was obtained by the 0.2% offset method.

For SS275, the mean elastic modulus (E) was 206.46 GPa and yield stress (F_y) was 293.29 MPa, which satisfies the limiting yield stress of

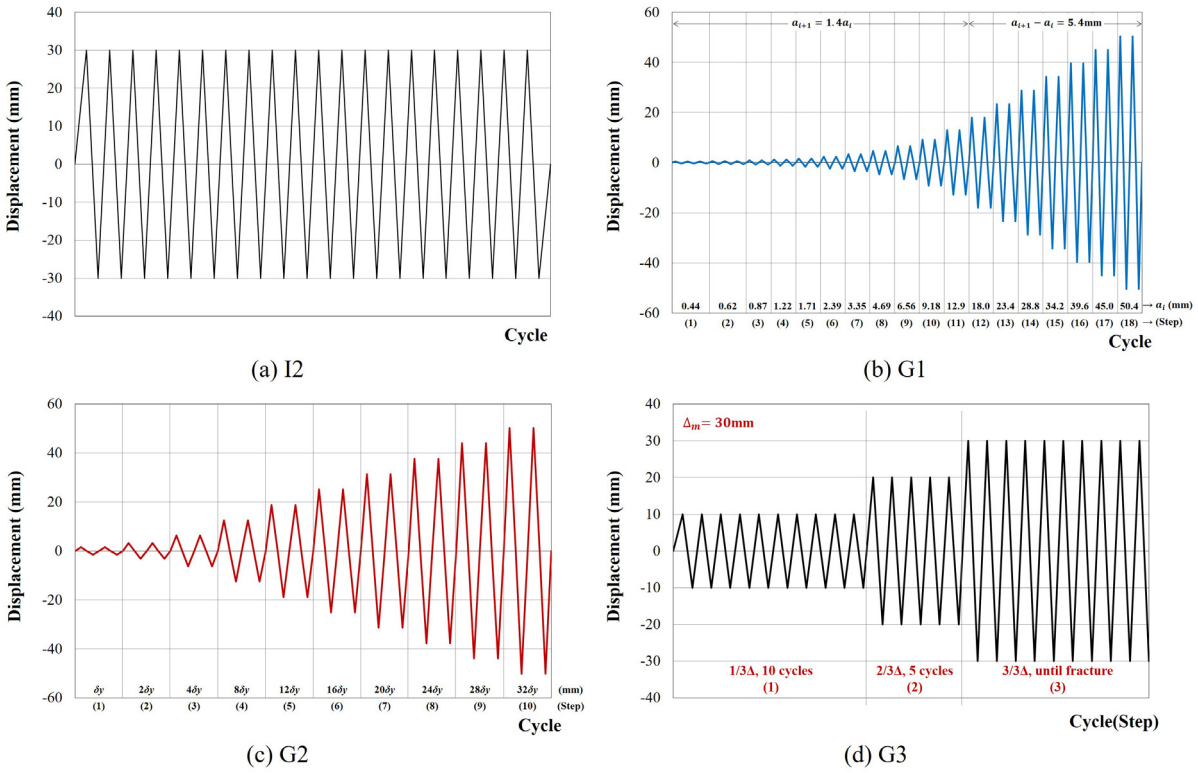

Fig. 2. Loading protocols.

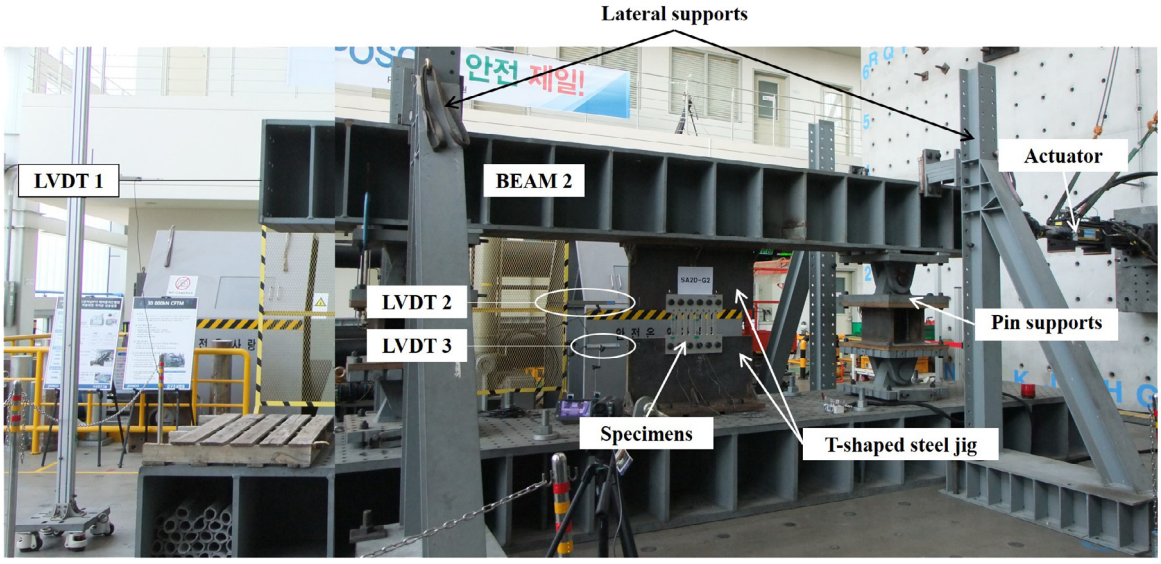

Fig. 3. Test set-up.

275 MPa specified in KS D 3503 [19], and the mean tensile strength (F_u) was 423.97 MPa, satisfying the required range of between 410 MPa and 550 MPa specified in KS D 3705 [18]. The mean elongation at fracture was 34.39%, which meets the minimum value of 18%. For STS316L, the value for E was 196.34 GPa; F_y was 275.85 MPa (1.58 times higher than the minimum yield stress of 175 MPa of KS D 3705 [17]); F_u was 576.66 MPa (1.20 times higher than the minimum tensile strength of 480 MPa of KS); and the elongation was 64.22%, which meets the requirement of more than 40% in KS.

Fig. 5 depicts the stress–strain relationship of the two steel materials obtained from the monotonic tensile test results. For the SS275 and STS316L materials used in the steel dampers, the F_y of STS316L was found to be approximately 6% lower than that of SS275, but the F_u of STS316L was 1.36 times that of SS275. The mean yield ratio (F_y/F_u) of STS316L was 47.84%, dramatically lower than the mean value (69.18%) of SS275. In addition, the ratio of the mean tensile strength to yield stress (F_u/F_y: strength enhancement) was 1.45 for SS275, but 2.09 for STS316L (Table 3) due to strong plastic strain hardening after yielding. STS316L also exhibited 1.87 times greater elongation (i.e., ductility) compared with SS275. This is because the differences in hardening effects between carbon steel and austenitic stainless steel may be attributed to the different crystal structures

Table 3
Material properties of SS275 and STS316L under monotonic loading.

Coupon name	Actual plate thickness t_e (mm)	Young's modulus E (GPa)	0.2% offset yield stress F_y (MPa)	Tensile strength F_u (MPa)	Yield ratio F_y/F_u (%)	Tensile to yield ratio F_u/F_y	Elongation at fracture EL (%)
SS275-1	13.70	206.68	292.58	421.64	69.39	1.44	34.00
SS275-2	13.71	205.10	293.45	423.18	69.34	1.44	34.76
SS275-3	13.70	207.62	293.85	427.09	68.80	1.45	34.43
Mean	13.70	206.46	293.29	423.97	69.18	1.45	34.39
COV	0.000	0.005	0.002	0.005	0.004	0.004	0.009
STS316L-1	13.16	196.84	275.31	577.81	47.65	2.10	65.23
STS316L-2	13.18	196.18	277.23	576.75	48.07	2.08	63.65
STS316L-3	13.18	196.02	275.02	575.43	47.79	2.09	63.78
Mean	13.17	196.34	275.85	576.66	47.84	2.09	64.22
COV	0.001	0.002	0.004	0.002	0.004	0.004	0.011

(Note) * Young's modulus ratio ($E_{ST.S316L}/E_{S.S275}$) = 0.95.
* Yield stress ratio ($F_{y-ST.S316L}/F_{y-S.S275}$) = 0.94.
* Tensile strength ratio ($F_{u-ST.S316L}/F_{u-S.S275}$) = 1.36.
* Elongation ratio ($EL_{-ST.S316L}/EL_{-S.S275}$) = 1.87.

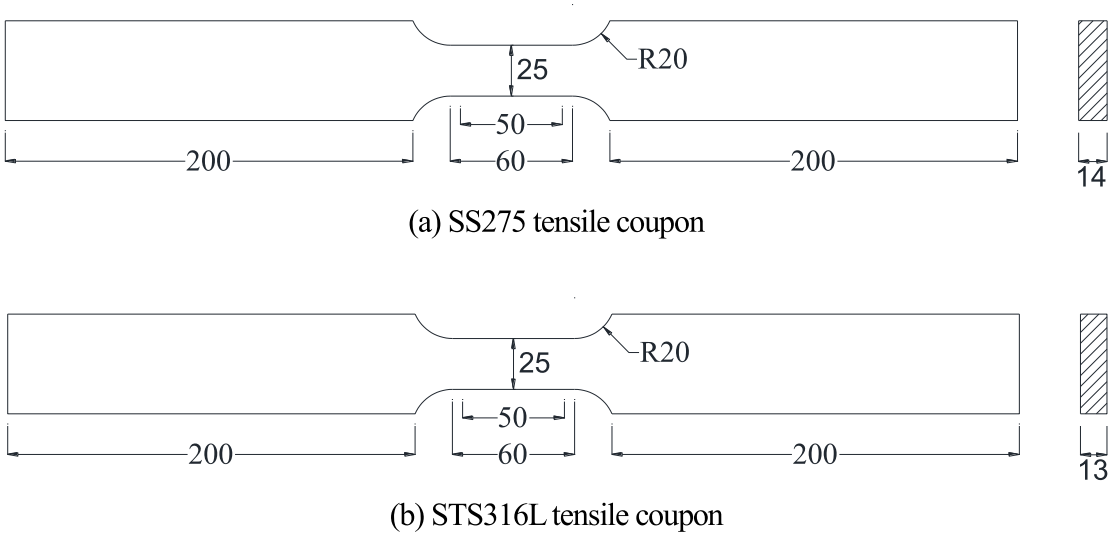

Fig. 4. Dimension of tensile coupons for monotonic tensile material test (Unit : mm).

(face-centered cubic, FCC, for austenitic stainless steel as opposed to body-centered cubic, BCC, for carbon steel, i.e., FCC metals tend to be more dense, stable and ductile than BCC metals) and alloy contents [Gardner].

2.5.2. Cyclic material test methods and results

During an earthquake, the steel slit damper is an energy dissipating element that is generally subjected to a relatively small number of cyclic loads accompanied by large plastic deformations over a short time, compared to members with small strain fatigue [29,30]. Therefore, the slit damper mainly depends on the geometric dimensions (the thickness, width and height of the strut) and the hysteretic behaviors of the material. Damper material properties can be studied by large-strain and low cycle fatigue tests. In this study, the cyclic material test continued until buckling or fracture of the specimen. In particular, the test was terminated due to the risk of damage to the testing machine caused by sudden buckling.

To experimentally investigate the hysteretic behavior of carbon steel SS275 and austenitic stainless steel STS316L, a cyclic material coupon test was performed according to ASTM E606/E606M [31] and KS B ISO 12106 [32].

Three round coupons with diameters of 6 mm and gauge lengths of 14 mm were fabricated for each material, as shown in Fig. 6(a). The test set-up for the cyclic tensile–compression test is shown in Fig. 6(b), and the test was performed at room temperature using an MTS810 machine. The strain rate was set to 0.005/s, and cyclic loading tests used a strain control mode with a perfectly symmetric triangular wave signal. An extensometer with a gauge length of 10 mm was installed on the coupon to measure displacement. The strain value was obtained by dividing the measured displacement by the gauge length (10 mm). Cyclic material tests were performed using three different loading protocols (Fig. 7). Three cyclic loading protocols were adopted, including the post-yield strain at which plastic deformation was expected based on data obtained from the monotonic tensile test results. As shown in Fig. 7(a), the P1 and P2 protocols specified constant strain amplitudes of 1% and 3%, respectively, repeated for 50 cycles. The P3 cyclic loading protocol was repeated twice with gradually increasing the strain by increments of 0.5% from ±0.5% to ±10.0%.

The ultimate shapes of each coupon after the tests are displayed in Fig. 8. For coupons SS275-P1 and STS316L-P1 with a strain constant amplitude of 1%, no buckling or failure was observed during cyclic loading. In other words, there was no strength reduction during cyclic loading. For coupons SS275-P2 and SS275-P3, tensile cracking and compressive buckling were observed visually during cyclic loading. STS316L-P2 and STS316L-P3 showed buckling and micro-cracking (which is not visible to the naked eye) due to excellent plastic deformation capacity after material yielding.

The stress–strain hysteresis curves and skeleton curves of the two steels are plotted in Figs. 9 and 10, respectively. It is known that

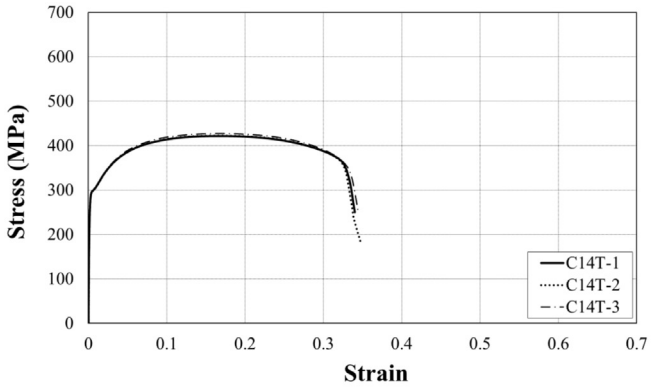

(a) SS275

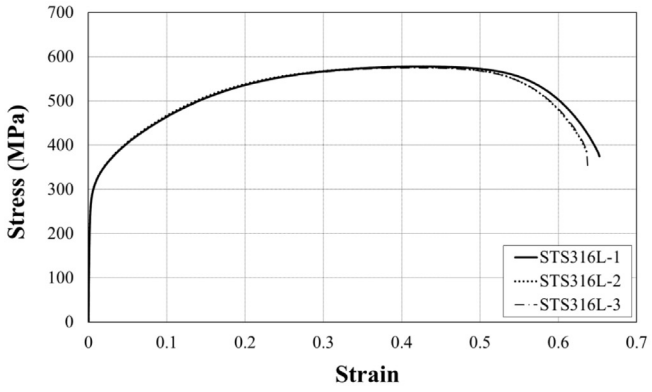

(b) STS316L

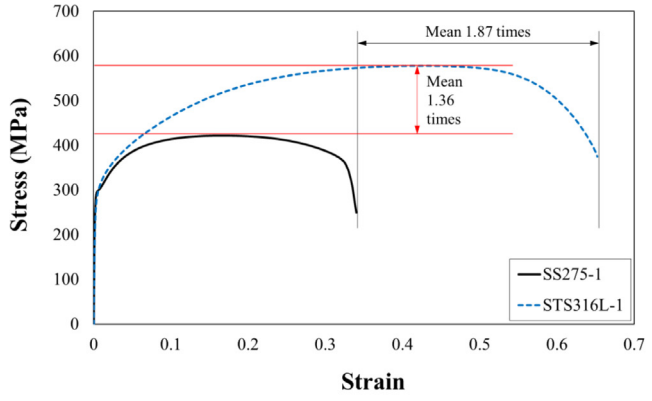

(c) Comparison of SS275-1 and STS316L-1

Fig. 5. Engineering stress–strain curves of material obtained from monotonic tensile coupon tests.

STS316L exhibited plumper hysteresis loops than carbon steel. In addition, the strength enhancement of STS316L material due to the noticeable cyclic hardening effect is significantly higher than that of the SS275, as can be seen in Fig. 10(c).

The cyclic coupon test results for SS275 and STS316L are summarized in Table 4. The yield stress, f_y values of the materials were determined using the 0.2% offset method. In Table 4, the average elastic modulus (E_c) and f_y of SS275 were 216.87 GPa and 360.34 MPa, respectively. In the case of STS316L, the E_c was 191.52 GPa and the f_y was 280.02 MPa. The value for maximum stress, $f_{u,max}$ in Table 4 was the larger value of maximum tensile stress (f_u^+) and maximum compressive stress (f_u^-) for cyclic test coupons with damage. The average ratio of maximum stress to yield strength ($f_{u,max}/f_y$, strength enhancement) of SS275 was 1.39, nearly identical to the mean value of 1.45 shown by the monotonic tensile coupon in Table 3. However,

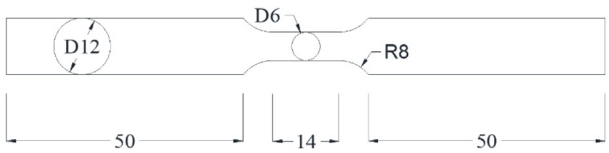

(a) Cyclic test round coupon

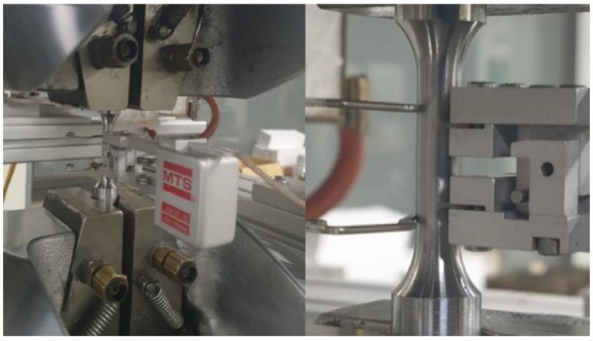

(b) Set-up for cyclic loading

Fig. 6. Cyclic coupon test coupon details and test set-up.

the average value of $f_{u,max}/f_y$ of STS16L-P2 and STS316L-P3 coupons was 2.82, approximately 1.35 times higher than the mean value of 2.09 (see Table 3) of the monotonic tensile coupon. In Table 4, because there was no tensile damage or compressive buckling for coupons SS275-P1 and STS316L-P1, those two coupons were excluded from the ultimate stress ($f_{u,max}$) comparison.

2.5.3. Comparison between stress–strain curve under monotonic loading and cyclic skeleton curve

Fig. 10 compares the monotonic tensile curves (for SS275-1 and STS316L-1 in Fig. 5) and skeleton curves for SS275-P3 and STS316L-P3 by cyclic material tests. In Tables 3 and 4, SS275 had a higher mean yield stress (=360.34 MPa) in cyclic test results than in the monotonic test results (a mean value of 293.29 MPa). For STS316L, there is no difference in the elastic modulus and yield stress between monotonic and cyclic test results. On the contrary, the mean maximum tensile stresses (787.94 MPa and 769.16 MPa, respectively) of STS316L-P2 and STS316L-P3 cyclic test coupons were 1.35 times larger than the monotonic tensile results (with a mean tensile strength of 576.66 MPa) due to cyclic hardening after yielding and ductile behavior due to TWIP, not TRIP, under cyclic loading.

3. Experimental results and comparison of seismic behavior

3.1. Number of cycles and fracture shapes

Figs. 11 and 12 show the fracture shapes of the SS275 (CS2D series) and STS316L (SA2D series) specimens, respectively, after the end of the test. For all specimens, cracks first appeared at the lower ends of the slit damper struts, followed by cracks at the upper ends of the struts, and the fatigue damage was consistently concentrated at cracked positions under cyclic loading. Table 5 summarizes the number of cycles prior to the initial crack and at the test end. In specimens CS2D-I2 and CS2D-I3, initial cracks were observed at 2 and 3 cycles, respectively, and the experiments were terminated at 3 and 5 cycles, respectively. Specimens CS2D-G1 and CS2D-G2 were terminated after 27 and 15 cycles, respectively, and initial cracks occurred at 25 and 13 cycles, respectively. For specimen CS2D-G3, the test was terminated at 13 cycles, and cracks occurred in all struts at 8 cycles. In specimen SA2D-I2, an initial crack occurred at 7 cycles, and the test was terminated after

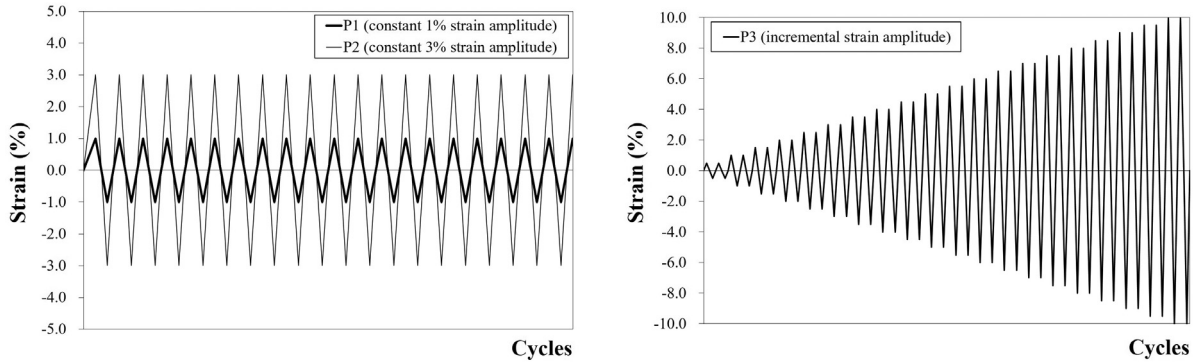

(a) Cyclic constant loading (P1 and P2) (b) Cyclic constant loading (P3)

Fig. 7. Cyclic loading protocol types for material test.

Table 4
Material properties of SS275 and STS316L under cyclic loading.

Coupon name	Actual diameter D_e (mm)	Elastic modulus Ec (GPa)	Yield stress f_y (MPa)	Yield strain ε_y (%)	Maximum tensile stress f_u^+ (MPa)	Maximum compressive stress f_u^- (MPa)	$f_{u,max}/f_y$	Failure mode
SS275-P1	6.00	217.61	360.83	0.3653	384.99	395.13	–	No failure
SS275-P2	6.00	219.19	362.60	0.3634	491.42	516.98	1.43	Buckling, Tensile crack
SS275-P3	6.00	213.82	357.59	0.3683	470.12	483.93	1.35	Buckling, Tensile crack
Mean	6.00	216.87	360.34	0.3657			1.39	
STS316L-P1	6.00	193.79	279.74	0.3449	460.50	473.72	–	No failure
STS316L-P2	6.00	187.69	280.84	0.3511	787.94	811.09	2.89	Buckling, micro crack
STS316L-P3	6.00	193.07	279.48	0.3449	769.16	743.34	2.75	Buckling, micro crack
Mean	6.00	191.52	280.02	0.3470			2.82	

(a) SS275

(b) STS316L

Fig. 8. Failure shapes of cyclic coupons at test ends.

10 cycles. For specimen SA2D-I3, initial cracks were observed at 13 cycles due to machining defects in the upper struts of Nos. 2 and 3. For specimen SA2D-G1, initial cracks appeared in all struts at 33 cycles. For specimens SA2D-G2 and SA2D-G3, initial cracks occurred at 20 cycles and 17 cycles, respectively. In summary, the number of cycles prior to the initial crack was higher in specimens having a loading protocol with a small displacement for each step, but the ultimate strength and the displacement at the crack decreased. Although a rapid loading speed increased the ultimate strength at the end of the test due to the cyclic hardening effect, it is thought that these tests were terminated early because the damage was accelerated. Moreover, when the number of cycles at crack initiation was compared between specimens SS275 and STS316L, STS316L dampers (the SA2D series) exhibited initial cracks after 5 to 10 more cycles than the SS275 dampers thanks to TWIP effects [17].

The experimental results show that austenitic stainless steel STS316L dampers exhibited stable and ductile behavior, not brittle, in contrast to the behavior of SS275 carbon steel and STS304 austenitic stainless-steel dampers described in previous reports [16]. Also, plastic deformation and visible necking in the critical section of the top and bottom of the struts were observed in Fig. 12, for example in the monotonic and cyclic material test results of STS316L. Molybdenum is added to STS316L stainless steel to destabilize the austenite, and nickel is also added to form a stable structure (Table 1) for corrosion resistance. According to studies by Shrinivas et al. [17] and Paul et el. [33], STS316 showed an intermediate TRIP behavior against deformation, and a higher fatigue performance than the STS304 steel. Consequently, as a seismic material, STS316L can improve stable hysteresis behavior and structural performance more effectively than can STS304. The austenite microstructure of STS316L is more stable than that of STS304, indicating STS316L materials experience few TRIP effects. Because this study focused on the applicability of stainless-steel dampers as seismic devices compared with carbon steel dampers, microstructure-related studies were not treated in this study.

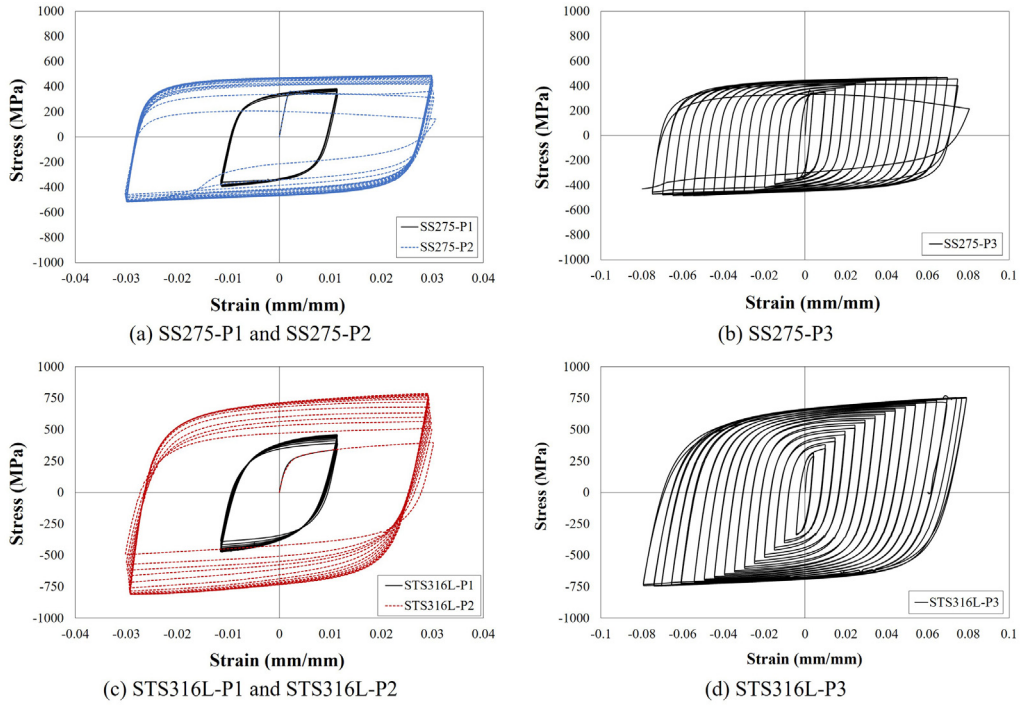

(a) SS275-P1 and SS275-P2 (b) SS275-P3

(c) STS316L-P1 and STS316L-P2 (d) STS316L-P3

Fig. 9. Cyclic hysteretic curves of coupons.

Table 5
Test results.

Specimen	Initial stiffness (kN/mm)	Second stiffness (kN/mm)	Stiffness ratio (%)	Ultimate strength		Maximum displacement		Number of cycle		Skeleton curve		Strength ratio	
				P_{ue}^{+} (kN)	P_{ue}^{-} (kN)	δ_{ue}^{+} (mm)	δ_{ue}^{-} (mm)	at test end	at crack initiation	Yield strength P_{ye} (kN)	Yield displacement δ_{ye} (mm)	$\alpha = P_{ue,max}/P_{ye}$	$\alpha_{SA2D}/\alpha_{CS2D}$
CS2D-M1	69.82	3.00	4.65	355.70		77.72				128.22	1.84	2.77	
CS2D-I2	67.59	3.07	4.54	217.90	209.02	30.19	29.99	3	2	131.17	1.94	1.66	
CS2D-I3	72.30	2.77	3.83	185.69	183.39	20.68	20.34	5	3	133.49	1.85	1.39	
CS2D-G1	72.84	1.99	2.73	168.78	163.54	18.20	17.86	27	25	136.34	1.87	1.24	
CS2D-G2	74.13	2.13	2.88	180.80	175.82	19.42	20.36	15	13	143.52	1.94	1.26	
CS2D-G3	76.31	3.85	5.04	173.48	167.97	20.10	12.65	13	8	128.64	1.69	1.35	
Mean	**72.63**	**2.76**	**3.95**							**134.63**	**1.86**	**1.38**	
COV	**0.044**	**0.273**	**0.275**							**0.043**	**0.056**	**0.123**	
SA2D-M1	72.65	3.65	5.03	482.19		90.57				101.45	1.40	4.75	0.92
SA2D-I2	62.41	3.61	5.79	252.95	246.14	30.23	30.91	10	7	103.73	1.66	2.44	1.47
SA2D-I3	61.60	3.23	5.24	233.32	225.74	20.30	20.30	21	13	108.67	1.76	2.15	1.54
SA2D-G1	68.21	3.23	4.73	269.42	258.64	39.84	39.58	34	33	147.86	2.17	1.82	1.47
SA2D-G2	60.26	3.03	5.03	265.82	251.43	39.38	31.67	22	20	154.13	2.56	1.72	1.37
SA2D-G3	62.77	4.01	6.38	251.10	244.51	31.07	30.09	21	17	102.76	1.64	2.44	1.81
Mean	**63.05**	**3.42**	**5.37**							**123.43**	**1.96**	**2.12**	**1.53**
COV	**0.048**	**0.114**	**0.122**							**0.205**	**0.203**	**0.159**	

* The mean value was calculated except for the M1 specimen.

3.2. Stiffness and strength

Skeleton curves obtained from cyclic loading tests presented in Fig. 13 were used to investigate the relative strength, stiffness, and deformation capacity of the specimens. The skeleton curves in Fig. 13 represent the load–displacement curves under one positive (+) loading cycle (tensile region) for I series specimens with constant-amplitude cyclic loading, and the curves were obtained by connecting the maximum load points at each loading step in the hysteretic curves for the G series specimens with incremental-amplitude cyclic loading [8,12,16].

Fig. 14 is a conceptual diagram for obtaining the stiffness (K_1 is initial stiffness and K_2 is secondary stiffness), yield strength (P_{ye}) and yield displacement (δ_{ye}), ultimate strength (P_{ue}) and maximum displacement (δ_{ue}) on skeleton curves. The P_{ye} and δ_{ye} of the dampers were determined to ensure that the dissipated energy capacity (area) under the skeleton curve obtained from the test was equal to the idealized bilinear curve, as indicated by the shaded areas in Fig. 14. The value for K_2 was defined as the slope that connects the yield strength, ultimate strength, and each displacement point. Fig. 15 shows the comparison of load–displacement hysteresis curves obtained under cyclic loading. The ▲ and ▽ marks indicate the ultimate strength locations in the CS2D series and SA2D series specimens, respectively. The SA2D series specimens exhibited greater strength compared with the CS2D series specimens at the same lateral displacement due to excellent strength enhancement after material yielding, similar to the results of the comparison of the stress–strain curves of the two steel materials shown in Fig. 3(c).

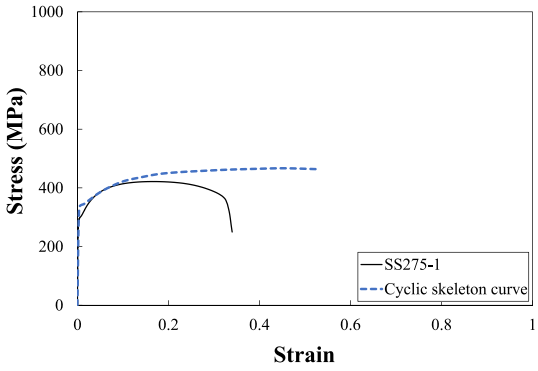

(a) SS275-1 and cyclic skeleton curve for SS275-P3

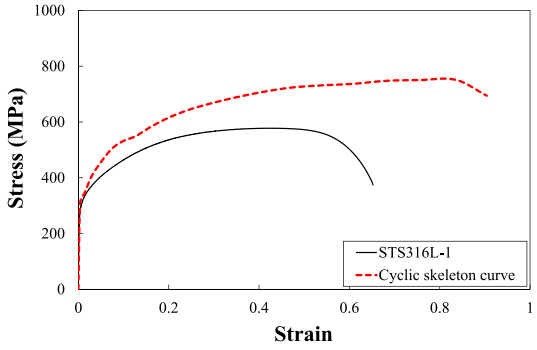

(b) STS316L-1 and cyclic skeleton curve for STS316L-P3

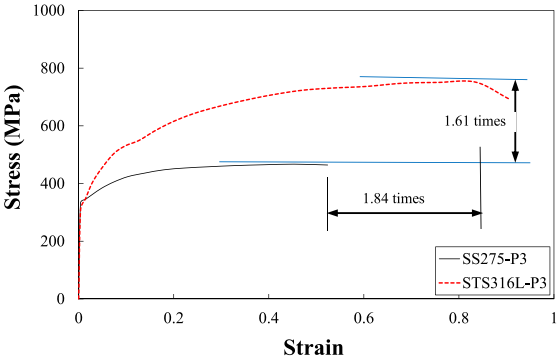

(c) Skeleton curves for SS275-P3 and STS316L-P3

Fig. 10. Comparison of monotonic tensile curves and cyclic skeleton curves.

The experimental values of specimens obtained from the skeleton curves are summarized in Table 5. The initial stiffness (K_1) of the STS316L dampers (SA2D series) was 13% lower than that of the SS275 dampers (CS2D series). The difference in initial stiffness, K_1, (average ratio 0.88) results from the difference in Young's modulus between STS316L and SS275 under cyclic loading, as shown in Table 4. In contrast, the K_2 value for the SA2D series specimens was 1.24 times higher than that of CS2D series specimens. For the CS2D series specimens, there was a big difference in the change according to cyclic loading protocols, as shown in Table 5. In the case of the SA2D series specimens, the average K_2 value was 3.42 and the deviation was lower than that of the CS2D series specimens regardless of loading protocols. Fig. 13(c) compares the skeleton curves of the two material types of specimens for the G1 and G2 loading protocols. STS316L dampers yielded earlier than the SS275 carbon steel dampers, exhibiting similar behavior until the displacement was less than 10 mm. The STS316L dampers exhibited considerable cyclic hardening due to plastic deformation after yielding, and the maximum displacement was approximately 51% higher than that of SS275 dampers.

The skeleton curves indicate that higher initial stiffness (K_1) and secondary stiffness (K_2) are more favorable in terms of energy dissipation capacity based on the same lateral displacement in the elastic region and the initial plastic hardening region. Generally, the K_2 must be lower than the K_1 of the main building to allow the seismic damper to absorb energy by in-plane deformation; therefore, the stiffness ratio (K_2/K_1) can be a crucial factor in estimating the seismic performance after the plastic region of the building system. In Table 5, the mean K_2/K_1 ratio is 3.95% for the CS2D series specimens and 5.37% for the SA2D series specimens, with the exception of the M1 specimens (Table 5). The K_2/K_1 ratio of the SA2D specimens was approximately 1.36 times higher than that of the CS2D specimens. The skeleton curves for the specimens of G series in Fig. 13(c) revealed that although STS316L dampers possess lower initial stiffness, their higher secondary stiffness, ductility, strength and cycle number after yielding compared with those of SS275 dampers result in higher seismic performance in terms of energy dissipation capacity.

For yield strengths of dampers from the skeleton curves of Fig. 13, even though the plate thickness and material yield stress of specimens SA2D-G1 and SA2D-G2 were lower than those of the CS2D specimens, the yield strengths of two specimens calculated were larger than those of CS2D-G1 and CS2D-G2 specimens, as can be seen in Table 5. However, for specimens with constant-amplitude cyclic loading, the SA2D-I series presented lower yield strengths compared with the CS2D-I series. The strength ratio ($\alpha = P_{ue,max}/P_{ye}$) was examined to investigate the strength enhancement by cyclic plastic hardening after yielding of the dampers. The maximum ultimate strength ($P_{ue,max}$) was the maximum of the ultimate strengths of the positive (+) and negative (−) regions in the hysteretic curves. The values for $P_{ue,max}/P_{ye}$ of the CS2D series and SA2D series were 1.38 and 2.12, respectively, in Table 5. These were similar to the tensile-to-yield ratios (F_u/F_y) of 1.45 and 2.09 shown in the monotonic material tensile test results in Table 3.

In addition, because the thicknesses of the specimens of the two steel materials were slightly different (see Table 2), the test strengths of specimens were corrected using a modification factor (m) based on a nominal plate thickness of 13 mm. Modified strengths for strength comparison are summarized in Table 6. The modification factor was calculated by dividing the nominal plate thickness by the measured plate thickness (t_e) included in Table 2 ($m = 13.0/t_e$). The average of the modified ultimate strengths (P_{uem}) of the SA2D series specimens was 1.53 times higher than that of the CS2D series specimens. The mean ultimate strength ratio of 1.53 (SA2D/CS2D from Table 6) was higher than the material tensile strength ratio of 1.36 ($F_{u-STS316L}/F_{u-SS275}$ from Table 3), due to the dominance of the cyclic hardening effect over the strain hardening effect under monotonic loading. In other words, in the cyclic material test results of coupons P2 and P3 with material damage, mean ultimate strength ratio ($f_{u,max-STS316L}/f_{u,max-SS275}$) was 1.55 in Table 4 and was close to the ultimate strength ratio of 1.53 (SA2D/CS2D) of dampers.

Fig. 16 displays the ultimate strength, which is defined as the peak load in each cycle under a constant-amplitude cyclic loading protocol. "PO" and "NE" in Fig. 16 denote the loading in the positive (+) and negative (-) directions, respectively. For the SA2D series specimens, the ultimate strength (peak load) tended to increase with the number of cycles due to the cyclic hardening effect, as shown in Fig. 15. SA2D-I series specimens with constant-amplitude testing exhibited no noticeable increase in ultimate strength even though the number of cycles increased. However, CS2D-I series specimens showed a rapid reduction in strength because the initiation and propagation of cracks in the upper and lower parts of the damper struts were accelerated at high amplitudes. This indicates that STS316L dampers provide stable and

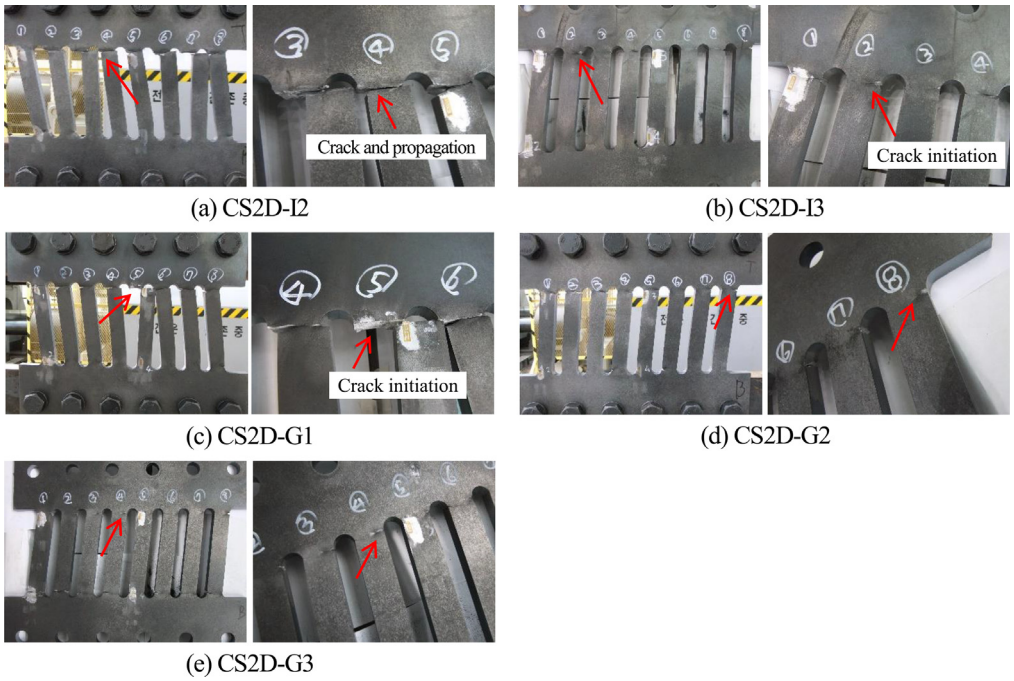

Fig. 11. Fracture shapes at test end (CS2D series).

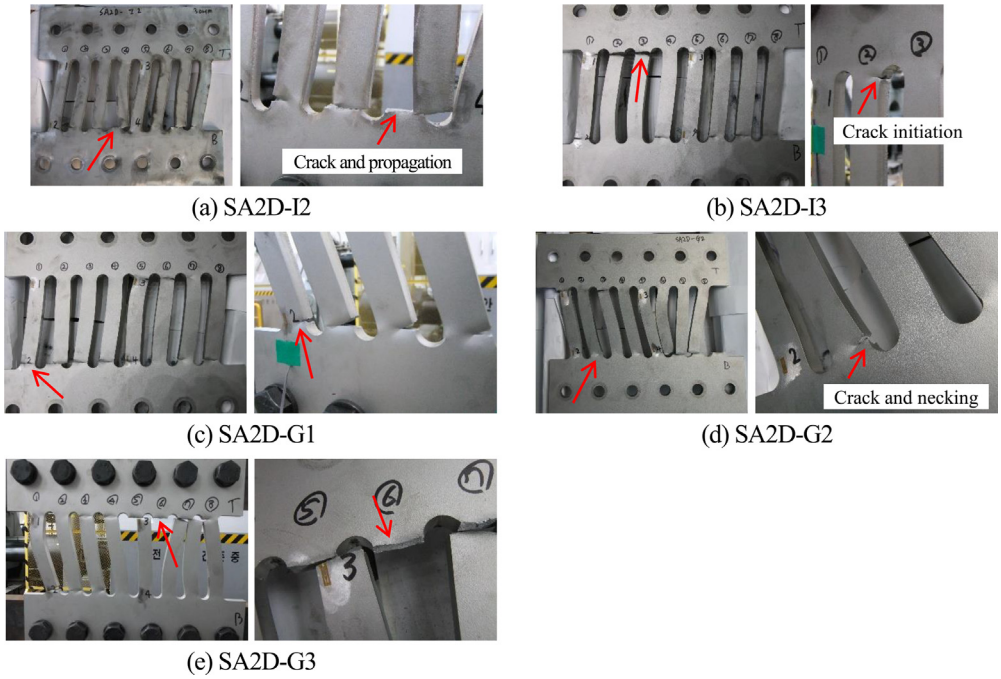

Fig. 12. Fracture shapes at test end (SA2D series).

superior seismic performance under high numbers of cycles compared to SS275 dampers.

3.3. Strain distribution

Four plastic strain gauges were attached to the struts of dampers in order to investigate the change in strain in the upper (SG1 and SG3) and lower (SG2 and SG4) parts according to the cyclic loading, as shown in Fig. 17(a). Figs. 17(b) and 17(d) show the cumulative displacement–strain relationship for two representative specimens CS2D-G1 and SA2D-I3. Figs. 17(c) and 17(e) present the displacement-strain relationship for specimens CS2D-I3 and SA2D-G1. The strain distributions at the top end (SG1 and SG3) of the struts of all specimens were similar to those at the bottom ends of the struts with no crack at the beginning step, as displayed in Figs. 17(c) and 17(e). As shown in Fig. 17(b) and (d), the tensile strain was higher than the compressive strain, and thus the intersecting points were slightly inclined to the positive region due to the increase of tensile strain caused by the membrane effect [11,16].

Table 6
Modification factor and test strength comparison.

Specimen	Modification Factor for damper thickness,	Modified ultimate strength		Modified yield strength (kN)	$P_{uem,max}/P_{yem}$	Strength ratio (SA2D/CS2D)		
		P_{uem}^{+} (kN)	P_{uem}^{-} (kN)			Positive (+)	Negative (−)	$P_{uem,max}/P_{pem}$
CS2D-I2	0.93	202.92	194.65	122.15	1.66			
CS2D-I3	0.93	173.42	171.27	124.67	1.39			
CS2D-G1	0.93	156.95	152.08	126.78	1.24			
CS2D-G2	0.93	168.61	163.96	133.85	1.26			
CS2D-G3	0.93	161.43	156.31	119.71	1.35			
Mean	**0.93**			**125.43**	**1.38**			
COV				**0.043**	**0.123**			
SA2D-I2	0.99	249.50	242.78	102.32	2.44	1.23	1.25	1.47
SA2D-I3	0.98	229.61	222.15	106.95	2.15	1.32	1.30	1.54
SA2D-G1	0.99	265.54	254.91	145.73	1.82	1.69	1.68	1.47
SA2D-G2	0.99	261.99	247.81	151.91	1.72	1.55	1.51	1.37
SA2D-G3	0.98	247.30	240.81	101.20	2.44	1.53	1.54	1.81
Mean	**0.99**			**121.62**	**2.12**	**1.47**	**1.45**	**1.53**
COV				**0.206**	**0.159**	**0.127**	**0.123**	**0.110**

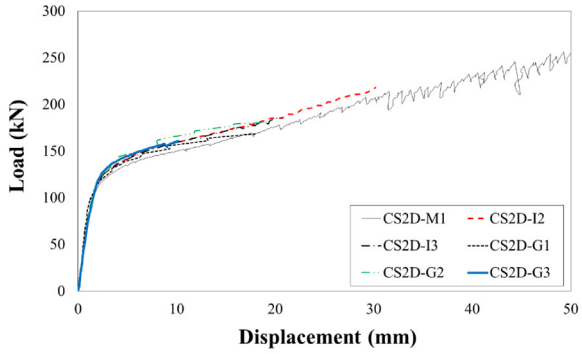

(a) CS2D series

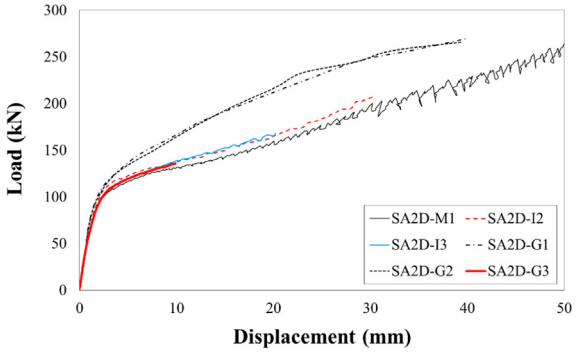

(b) SA2D series

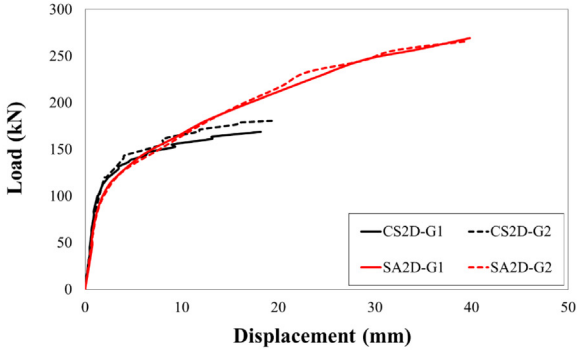

(c) CS2D-G series and SA2D-G series

Fig. 13. Skeleton curves.

3.4. Ductility and energy dissipation capacities

Table 7 summarizes the displacement, ductility and energy dissipation capacity of the specimens calculated from cyclic tests. The plastic deformation capacity of the steel damper was evaluated using ductility ($\mu = \delta_{ue,max}/\delta_{ye}$) and cumulative ductility ($\eta = \sum \delta_{ue}/\delta_{ye}$). Ductility ($\mu$) is the ratio of maximum displacement ($\delta_{ue,max}$) to yield displacement (δ_{ye}), and cumulative ductility (η) is the sum of all displacements ($\sum \delta_{ue}$) in the positive and negative directions up to the cycle at the time of initial cracking against yield displacement (δ_{ye}). In the case of the steel dampers under cyclic loading, the value of η in both directions becomes a more important index than μ in one direction. The SA2D series (STS316L) specimens showed up to 1.89 times higher ductility (μ) than CS2D series specimens. The SA2D series specimens experienced plastic deformation exceeding 500 times the yield displacement before cracking initiated. The cumulative ductility (η) for the SA2D series specimens was 3.20 times higher, on average, than that of the CS2D series specimens.

The energy dissipation capacity (E_t) can be calculated by adding the loop area of the load–displacement curves. As shown in Table 7, total energy dissipation capacity (E_{tf}) is the calculated loop area for the total number of cycles until the end of the experiment, and E_{tc} is the calculated loop area up to the cycle in which the initial crack occurs. At the end of the test, total energy dissipation capacity, E_{tf}, of the SA2D series specimens was on average 4.03 times higher than that of the CS2D series specimens. Also, the average energy absorption capacity (E_{tc}) in the initial crack occurrence of the SA2D series specimens was 5.07 times higher than that of the CS2D specimens due to excellent strength enhancement and ductility, and higher number of cycles until test end. Fig. 18 shows the energy dissipation capacity for each cycle based on the same loading protocol in all specimens. The energy dissipation capacity of the SA2D series specimens was up to 7.78 times larger than that of the CS2D specimens until initial cracks occurred at the top and bottom ends of the dampers. Fig. 19 shows the ratios (E_{tfSA}/E_{tfCS} and E_{tcSA}/E_{tcCS}) of the energy dissipation capacity of SA2D series specimens to those of CS2D series specimens. To further investigate the energy dissipation capacity of specimens, normalized energy dissipation capacity is presented in Fig. 20 in the form of $E_{tf}/(P_{ye}\delta_{ye})$. The normalized energy dissipation capacity can be defined as a non-dimensional value by dividing the total energy dissipation capacity (E_{tf}) by the elastic energy dissipation capacity ($P_{ye}\delta_{ye}$). The normalized energy dissipation capacity of the SA2D series specimens was on average 4.38 times larger than that of the CS2D series specimens. The austenitic stainless steel STS316L dampers experienced noticeable cyclic hardening at every loading cycle, and they also provided higher secondary stiffness and ductility, and sufficient

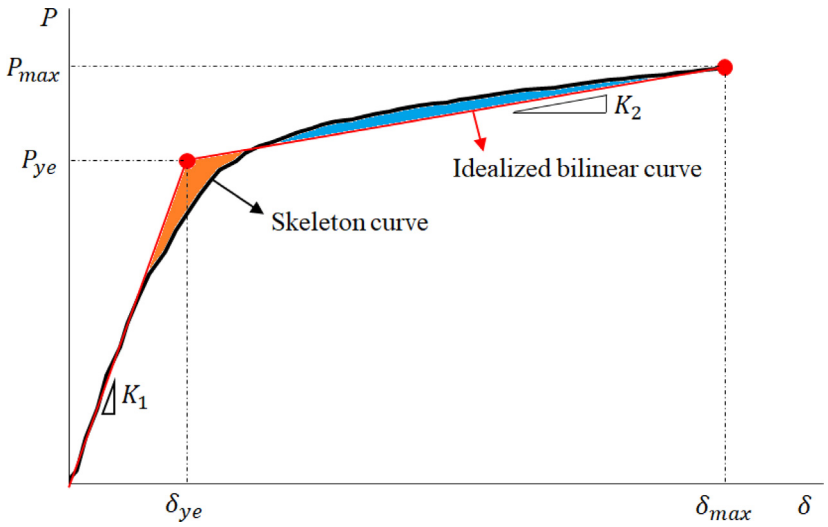

Fig. 14. Yield strength (P_{ye}) and yield displacement (δ_{ye}) in the skeleton curve.

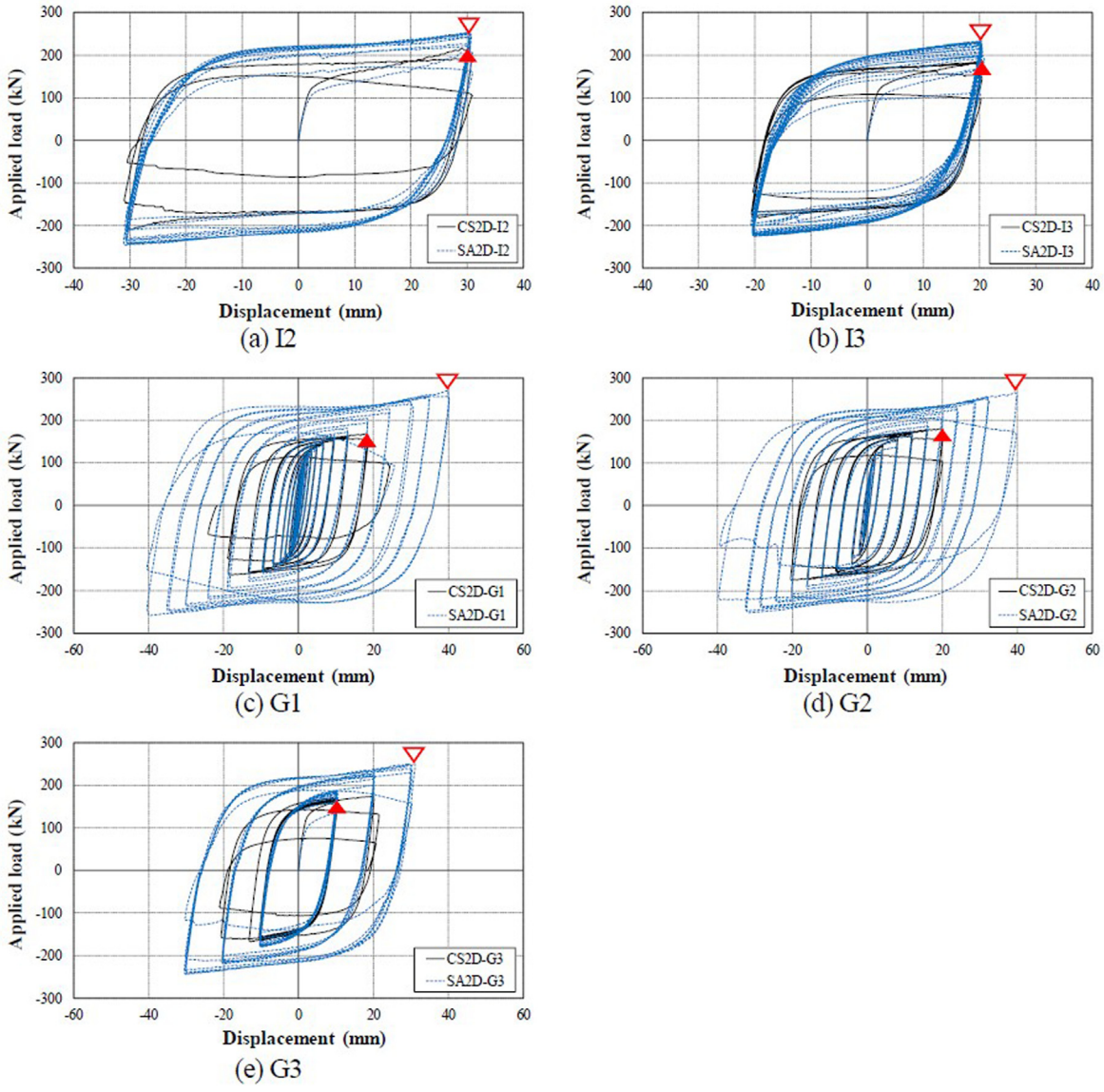

Fig. 15. Comparison of hysteresis curves.

Table 7
Ductility and energy dissipation capacity.

Specimen	Displacement and ductility						Total energy dissipation capacity E_t				Normalized energy dissipation capacity	
	Maximum displacement (mm)	Cumulative displacement at crack (mm)	Ductility, μ		Cumulative ductility, η		At test end		At initial crack			
			$\delta_{ue,max}/\delta_{ye}$	SA2D/CS2D	$\sum\delta_{ue}/\delta_{ye}$	SA2D/CS2D	E_{tf} (kN m)	SA2D/CS2D	E_{tc}(kN m)	SA2D/CS2D	$E_{tf}/(P_{ye}\delta_{ye})$.	SA2D/CS2D
CS2D-I2	30.19	342.16	15.56		176.32		45		33		176	
CS2D-I3	20.68	351.03	11.20		190.12		45		20		183	
CS2D-G1	18.20	603.75	9.72		322.57		54		38		212	
CS2D-G2	20.36	537.23	10.52		277.48		59		46		214	
CS2D-G3	20.10	612.58	11.92		363.36		66		37		304	
SA2D-I2	30.91	1203.85	18.60	1.20	724.32	4.11	207	4.60	145	4.40	1199	6.80
SA2D-I3	20.30	1692.19	11.51	1.03	959.12	5.04	241	5.36	157	7.78	1259	6.89
SA2D-G1	39.84	1530.05	18.38	1.89	705.81	2.19	234	4.32	204	5.36	730	3.44
SA2D-G2	39.38	1480.89	15.40	1.46	578.97	2.09	228	3.83	176	3.88	577	2.70
SA2D-G3	31.07	1515.94	18.98	1.59	925.95	2.55	224	3.40	145	3.95	1331	4.38
Mean				1.43		3.20		4.03		5.07		4.84

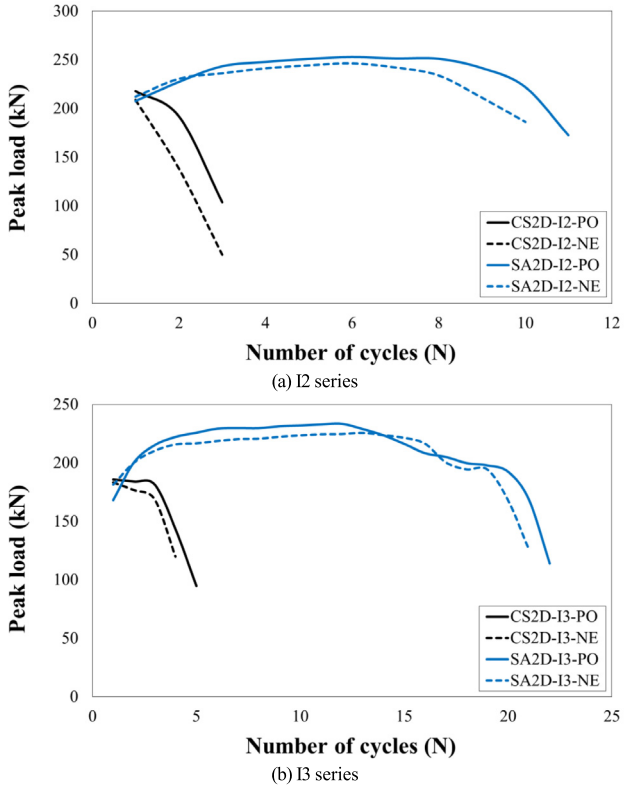

Fig. 16. Peak load according to each cycle for constant amplitude loading protocol.

enhancement strength after yielding due to the TWIP effect under cyclic loading.

3.5. Comparison of theoretical predictions and test results

3.5.1. Design concept of slit damper

When horizontal force is applied to a steel slit damper, bending moment and shear force are generated in the strut of the slit damper. As the aspect ratio (the height-to-width ratio of the strut) increases, the ultimate behavior of the damper is governed by flexure. In this study, a simple flexure-dominant slit damper with an aspect ratio of 5.0 was designed so that shear could be ignored. One strut can be simplified as a model with both ends fixed, as shown in Fig. 21. The theoretical model of the steel slit damper was derived from studies conducted by Lee et al. [12] and Ma et al. [34]. Based on the rectangular cross-section of the strut end, the plastic moment (M_p) can be calculated by the following equation:

$$M_p = F_y Z = F_y t B^2/4 \tag{1}$$

where Z is the plastic section modulus of the strut, F_y is the yield stress of the material, t is the strut thickness, and B is the strut width, as shown in Fig. 1.

The horizontal force when the strut end reaches the plastic moment (M_p) denotes the plastic strength (P_p) of the damper. The relationship of Eq. (2) is established by the condition of the moment equilibrium, and Eq. (3) can be obtained by substituting into Eq. (1). Because the cross-section of the strut is rectangular, the yield strength, P_y can be obtained from Eq. (4) using the shape factor, expressed as the ratio of plastic section modulus (Z) to elastic section modulus (S), which is 1.5.

$$M_p = P_p h/2 \tag{2}$$

$$P_p = 2F_y t B^2/4h \tag{3}$$

$$P_y = 2F_y t B^2/6h \tag{4}$$

For a steel slit damper composed of multiple struts, the horizontal force is distributed evenly among the struts. The whole strength of the damper can therefore be calculated by multiplying the theoretical strength of one strut by the number of struts.

3.5.2. Predictive formulas in previous studies

The structural performances of steel slit dampers are included in Table 8 by applying the design formulas of yield strength, P_{yt}, and yield displacement, δ_{yt}, [11–14] and seismic structure design guidelines [25,26]. Because shear and bending deformations occur simultaneously in the structural element subjected to horizontal shear force, the smaller of the yield strength $P_{b,yt}$ by bending and $P_{s,yt}$ by shear force can be used to predict the P_{yt} of a steel slit damper in the following equations:

$$P_{b,yt} = \frac{tB^2F_y}{2H'} \tag{5}$$

$$P_{s,yt} = \frac{2}{3}\frac{tBF_y}{\sqrt{3}} \tag{6}$$

$$P_{yt} = n \times Min(P_{b,yt}, P_{s,yt}) \tag{7}$$

where t is the thickness of the damper, n is the number of struts, B is the strut width, H is the height of the straight strut part, H' is derived from $H + 2r^2/H_T$, H_T is defined as $H + 2r$, r is the radius of the strut end, and F_y denotes the yield stress of the material.

The yield displacement of the damper (δ_{yt}) can be calculated with the following equation on the sum of the yield deformation by bending and shear force:

$$\delta_{yt} = \frac{1.5P_yH_T}{nEtB}\left[\left(\frac{H'}{B}\right)^2 + 2.6\right] \tag{8}$$

where E is the Young's modulus of the material.

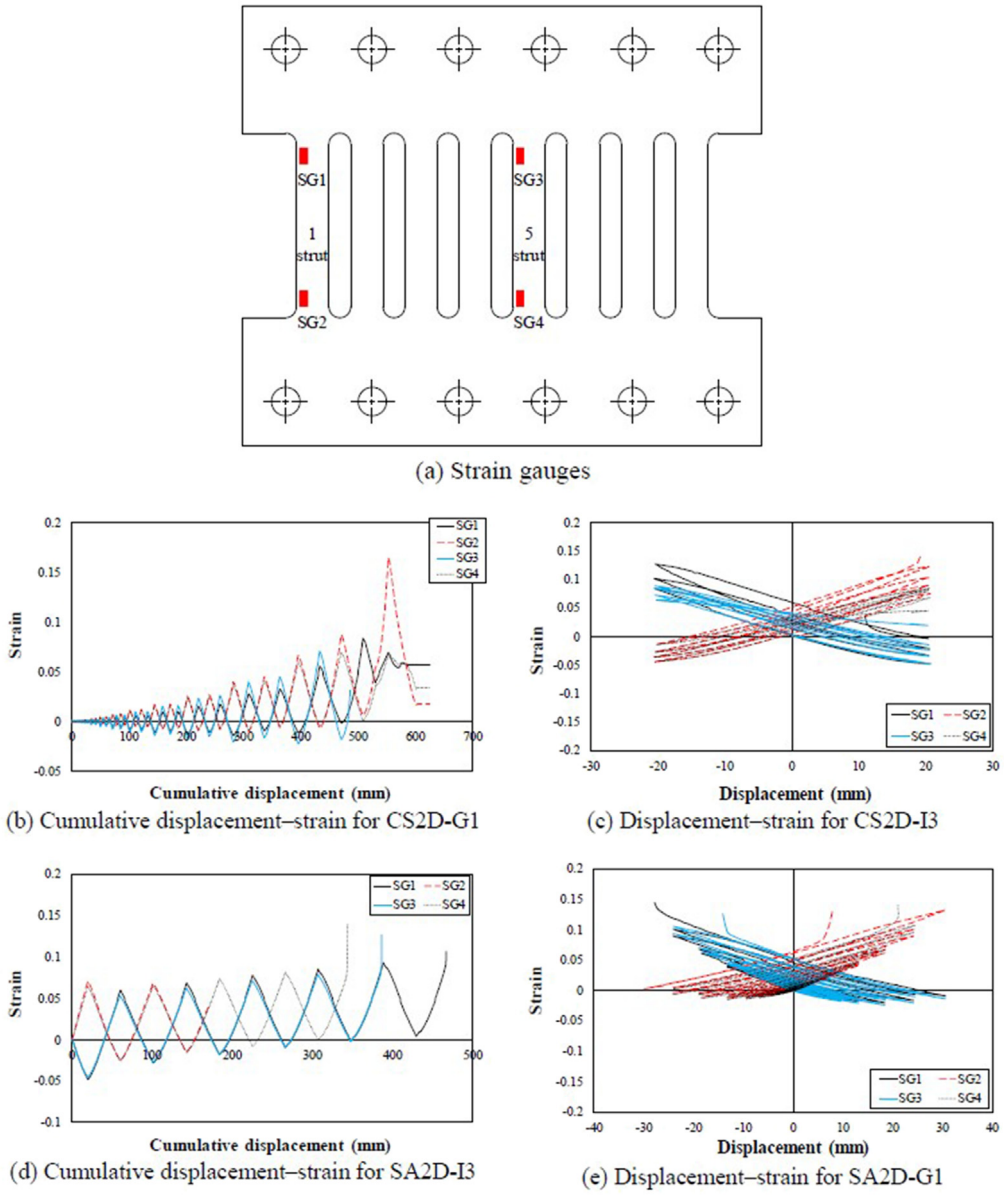

(a) Strain gauges

(b) Cumulative displacement–strain for CS2D-G1

(c) Displacement–strain for CS2D-I3

(d) Cumulative displacement–strain for SA2D-I3

(e) Displacement–strain for SA2D-G1

Fig. 17. Displacement-strain relationship the both ends of struts.

Table 8
Comparison of test results and theoretical predictions.

Specimen	Test results				Theoretical predictions			K_1/K_e	P_{ye}/P_{yt}	δ_{ye}/δ_{yt}	$P_{ue.max}/P_{yt}$	Modified energy dissipation capacity and ratio	
	Initial stiffness K_1(kN/mm)	Yield strength P_{ye} (kN)	Yield displacement δ_{ye} (mm)	Ultimate strength $P_{ue.max}$ (kN)	Elastic stiffness K_e(kN/mm)	Yield strength P_{yt} (kN)	Yield displacement δ_{yt} (mm)					E'_{tf} (kN m)	SA2D/ CS2D
CS2D-I2	67.59	131.17	1.94	217.90	95.91	96.79	1.01	0.70	1.36	1.92	2.25	45	
CS2D-I3	72.30	133.49	1.85	185.69	96.26	96.96	1.01	0.75	1.38	1.83	1.92	45	
CS2D-G1	72.84	136.34	1.87	168.78	96.23	97.05	1.01	0.76	1.40	1.85	1.74	55	
CS2D-G2	74.13	143.52	1.94	180.80	96.04	96.84	1.01	0.77	1.48	1.92	1.87	60	
CS2D-G3	76.31	128.64	1.69	173.48	95.98	96.86	1.01	0.80	1.33	1.67	1.79	67	
Mean	72.17	134.63	1.86		96.08 (97.18)	96.90 (97.78*)	1.01 (1.01)	0.76	1.39	1.84	**1.91**		
SA2D-I2	62.41	103.73	1.66	252.95	85.87	85.77	1.00	0.73	1.21	1.66	2.95	206	4.54
SA2D-I3	61.60	108.67	1.76	233.32	86.30	86.14	1.00	0.71	1.26	1.76	2.87	239	5.27
SA2D-G1	68.21	147.86	2.17	269.42	86.82	86.47	1.00	0.79	1.71	2.17	3.31	231	4.23
SA2D-G2	60.26	154.13	2.56	265.82	86.74	86.41	1.00	0.69	1.78	2.56	3.27	225	3.74
SA2D-G3	62.77	102.76	1.64	251.10	86.97	86.59	1.00	0.72	1.19	1.64	3.08	221	3.32
Mean	64.65	123.43	1.96		86.54 (85.82)	86.28 (85.40*)	1.00 (1.00)	0.73	1.43	1.96	**3.13**		4.22

* : The value in parentheses () is the reference yield strength (P_{yr}) based on the nominal dimensions of the damper, strut number and the material yield stress obtained from the monotonic tensile material test.

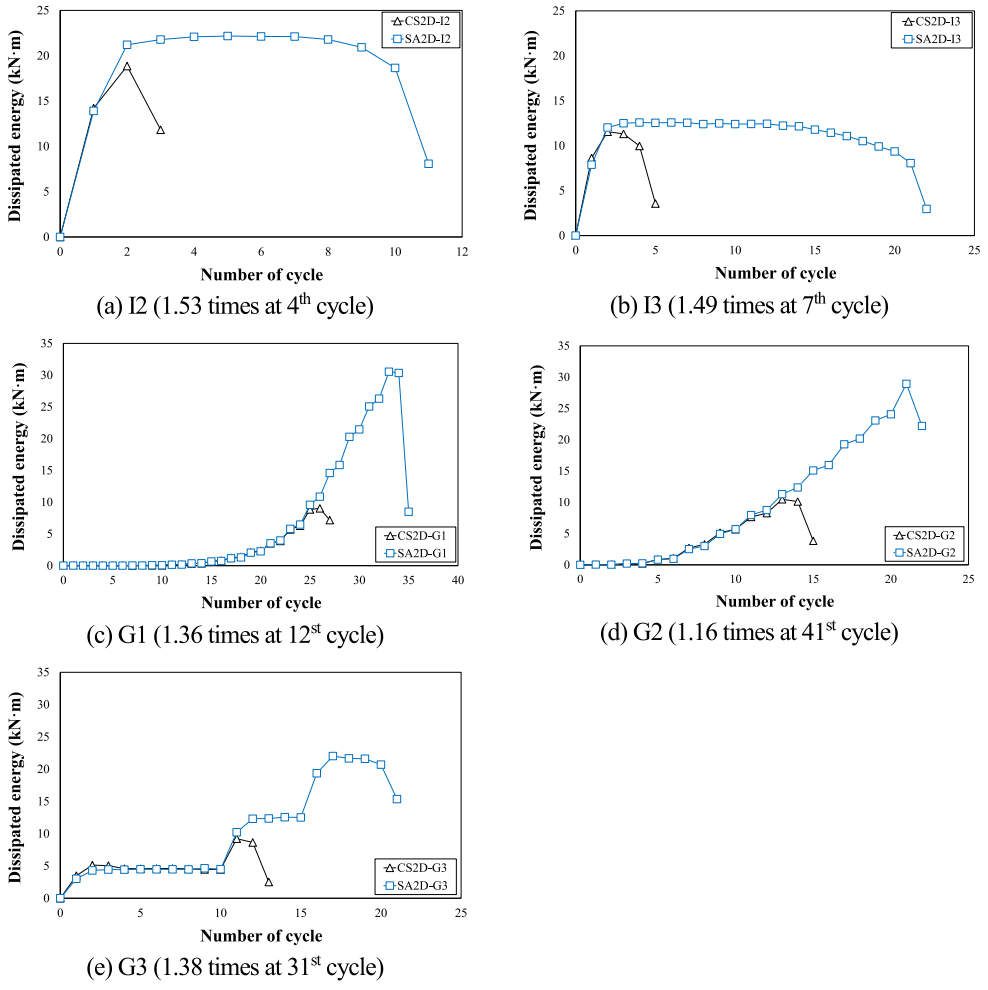

Fig. 18. Energy dissipation capacity according to each cycle.

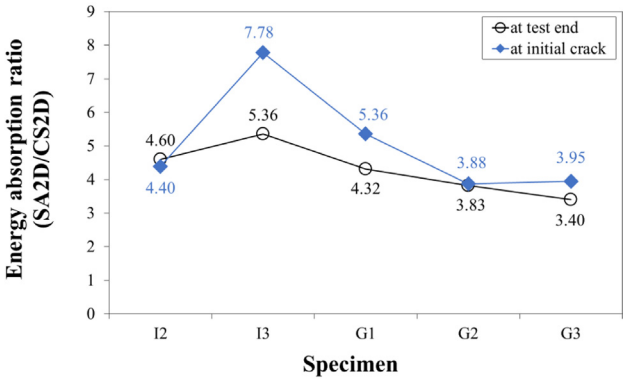

Fig. 19. Comparison of total energy absorption between SA2D series and CS2D series specimens.

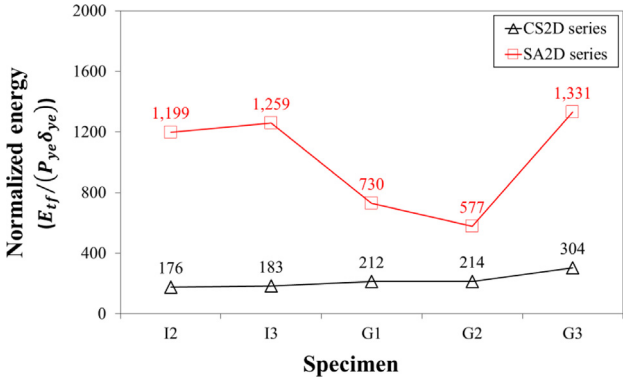

Fig. 20. Normalized energy dissipation capacity between SA2D series and CS2D series specimens.

The elastic stiffness (K_e) of the damper is the ratio of yield strength (P_{yt}) to yield displacement (δ_{yt}) using Hook's law,

$$K_e = \frac{P_{yt}}{\delta_{yt}} \tag{9}$$

K_e, P_{yt}, and δ_{yt} of each damper were calculated by applying the geometric dimensions in Table 2 and the material test results in Table 3. Table 8 includes stiffness (K_1, K_e), yield strength (P_{ye}, P_{yt}), ultimate strength ($P_{ue.max}$) and yield displacement (δ_{ye}, δ_{yt}) obtained in both test results and theoretical predictions.

3.5.3. Comparison of test results and theoretical predictions

Table 8 also summarizes the comparisons of theoretical predictions and test results for all specimens. Predicted values were calculated for elastic stiffness (K_e), yield strength (P_{yt}), and yield displacement (δ_{yt}). The ratios (K_1/K_e) of initial stiffness (K_1) to elastic stiffness (K_e)

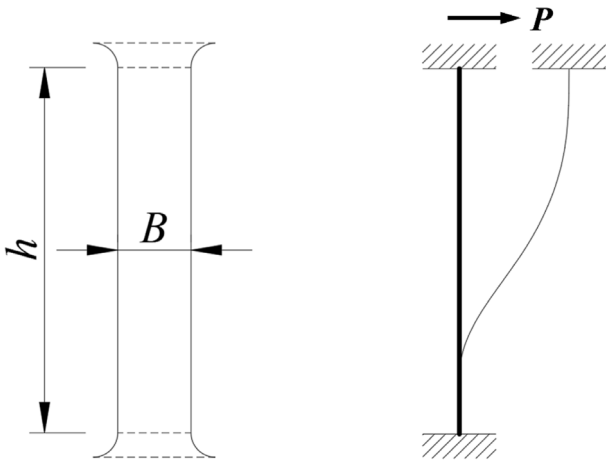

Fig. 21. Shape of the strut and deformed shape.

ranged from 0.69 to 0.80, indicating that initial stiffness test results were lower than the values calculated in the above equation due to geometric imperfections of the damper and end fixity of the set-up. Factors such as imperfections and end fixity in test specimens resulted in initial stiffness reduction and yield displacement increase.

Fig. 22 shows the normalized load ($P_{ue,max}/P_{yt}$) of the ultimate strength ($P_{ue,max}$) of each specimen against the predicted value for P_{yt} by Eq. (3) and the mean ratio (F_u/F_y) of tensile strength to yield stress (Table 3). According to Lee et al. [12] and Hwang et al. [16], '①' in Fig. 22 denotes the strength enhancement (F_u/F_y = 1.45) expected by strain hardening after material yielding. Because vertical deformation is restrained in the upper and lower struts of the dampers, the tensile resistance due to elongation in the longitudinal direction becomes significant in the range of large displacement. Therefore, external loads are resisted by a combination of flexure and tension. This phenomenon is called the membrane effect. '②' in Fig. 22 represents the increase in ultimate strength due to the membrane effect and cyclic hardening. The $P_{ue.max}/P_{yt}$ values ranged from 1.74 to 2.25 (with a mean of 1.91) for the CS2D series specimens and from 2.97 to 3.31 (with a mean of 3.13) for the SA2D series specimens, which were larger than the mean F_u/F_y ratio (1.45 and 2.09, respectively) in material test results. Moreover, the P_{ye}/P_{yt} ratio of the measured yield strength, P_{ye}, to predicted yield strength, P_{yt}, ranged from 1.21 to 1.48, except for specimens SA2D-G1 and SA2D-G2. In contrast, the P_{ye}/P_{yt} ratios of specimens SA2D-G1 and SA2D-G2 were 1.71 and 1.78, respectively. This is because the yield strength increased rapidly near the target displacement for each cycle without any damage due to strong cyclic plastic hardening and membrane effects after yielding, as discussed in Lee et al. [12] and Hwang et al. [16]. In addition, since the material properties and plate thickness in the damper specimens are different, modified energy-dissipation capacity (E'_{tf}) was obtained by multiplying the total E_{tf}

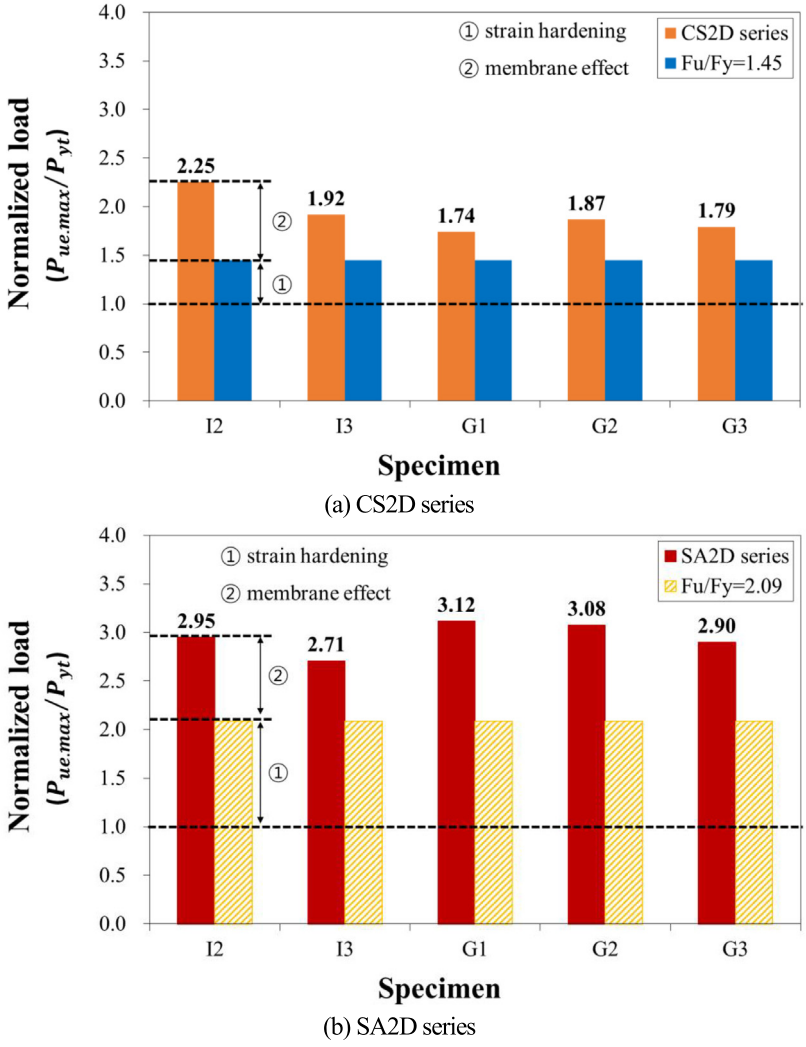

Fig. 22. Strength increase due to strain hardening and membrane effect.

at test end by the ratio of the reference yield strength (P_{yr}) to the calculated yield strength (P_{yt}) from Table 8 of each specimen, making it possible to compare the energy absorptions of each specimen under identical conditions. As already stated in Section 3.5, the modified energy dissipation capacity of the SA2D series specimens was also 4.22 times larger, on average, than that of the CS2D series specimens thanks to stable hysteretic behavior and excellent enhancement strength after yielding due to the TWIP effect under cyclic loading

4. Conclusions

Steel slit dampers for seismic retrofits were designed and fabricated using austenitic stainless steel (STS316L, equivalent to ASTM 316L type) and mild carbon steel (SS275, equivalent to ASTM A36), and cyclic loading tests were conducted under various protocols. Material properties, hysteretic behavior and energy-dissipation capacity were compared. The following conclusions can be drawn.

(1) The yield stress of STS316L was approximately 6% lower than that of SS275, and the tensile strength was 1.36 times higher than that of SS275. Stainless steel STS316L also showed 1.87 times greater elongation (ductility) and 1.44 times greater mean tensile strength to yield stress ratio (strength enhancement) compared with SS275. The strength enhancement of cyclic test results for STS316L material was 35% higher than that of the monotonic tensile test due to significant cyclic hardening. Both material test results indicated that the energy-dissipation capacity of STS316L is superior to that of SS275.

(2) The behavior of the steel dampers under monotonic loading protocol tended to be similar to the material tensile test results. The number of cycles at test end and at crack initiation for most of the STS316L specimens under cyclic loading was larger compared to the SS275 specimens. The mean strength ratio for the dampers corresponded to that of the ratio of tensile strength to yield stress at the material level. The STS316L damper with added molybdenum (Mo) and higher nickel (Ni) contents showed ductile behavior thanks to the TWIP effect, whereas the test results of STS304 damper exhibited brittle fracture due to the TRIP effect.

(3) STS316L (SA2D series) dampers experienced significant cyclic hardening due to plastic deformation and exhibited a ductile fracture shape due to initial cracking at a larger displacement compared with the SS275 specimens. The STS316L specimens showed up to 1.89 times the ductility, and 3.20 times the cumulative ductility, of the SS275 specimens. At the initial cracking step, the energy-absorption capacity of the STS316L dampers was approximately 5.07 times higher than that of the SS275 dampers. The normalized energy dissipation capacities with identical geometric information of the STS316L dampers were on average 4.38 times higher than those of the SS275 dampers. Therefore, STS316L slit dampers can provide superior energy dissipation as seismic devices in a building structure compared to mild carbon steel dampers due to their excellent ductility and strength enhancement.

In the near future, based on the material properties and experimental results determined under cyclic loading in this study, a finite element analysis model will be developed to examine the mechanism of cyclic strain hardening and membrane effects in detail.

CRediT authorship contribution statement

BoKyung Hwang: Writing – original draft, Methodology, Investigation. **TaeSoo Kim:** Writing – review & editing, Validation, Supervision, Project administration, Funding acquisition, Data curation, Conceptualization. **YongHan Ahn:** Writing – review & editing, Validation, Funding acquisition.

Declaration of competing interest

The authors declare that they have no known competing financial interests or personal relationships that could have appeared to influence the work reported in this paper.

Data availability

The authors do not have permission to share data.

Acknowledgments

This work was supported by the research fund of Hanyang University (HY-2022-1428), Republic of Korea and the research fund of Hanyang University (HY-2022-0900), Republic of Korea. Cyclic tests of specimens were conducted at the Steel Structure Laboratory of POSCO. Authors sincerely appreciate their help with the experiments.

References

[1] L. Gardner, The use of stainless steel in structures, Prog. Struct. Eng. Mater. 7 (2) (2005) 45–55.
[2] G. Gedge, Structural uses of stainless steel—buildings and civil engineering, J. Construct. Steel Res. 64 (11) (2008) 1194–1198.
[3] N.R. Baddoo, Stainless steel in construction: A review of research, applications, challenges and opportunities, J. Construct. Steel Res. 64 (11) (2008) 1199–1206.
[4] B. Rossi, Discussion on the use of stainless steel in constructions in view of sustainability, Thin-Walled Struct. 83 (2014) 182–189.
[5] The Steel Construction Institute (SCI), Design Manual for Structural Stainless Steel, fourth ed., SCI, Silwood Park, Ascot, Berkshire. SL5 7QN, UK, 2017.
[6] K.H. Nip, L. Gardner, C.M. Davies, A.Y. Elghazouli, Extremely low cycle fatigue tests on structural carbon steel and stainless steel, J. Construct. Steel Res. 66 (1) (2010) 96–110.
[7] K.H. Nip, L. Gardner, A.Y. Elghazouli, Cyclic testing and numerical modelling of carbon steel and stainless steel tubular bracing members, Eng. Struct. 32 (2) (2010) 424–441.
[8] F. Zhou, C. Fang, Y. Chen, Experimental and numerical studies on stainless steel tubular members under axial cyclic loading, Eng. Struct. 171 (2018) 72–85.
[9] R.H. Kim, T.S. Kim, S.H. Lim. Y. Xi, Hysteretic behavior comparison of austenitic and lean duplex stainless steel square hollow section members under cyclic axial loading, Eng. Struct. 237 (2021) 112227.
[10] L.D. Sarno, A.S. Elnashai, D.A. Nethercot, Seismic response of stainless steel braced frames, J. Construct. Steel Res. 64 (7–8) (2008) 914–925.
[11] C.H. Lee, Y.K. Ju, J.K. Min, S.H. Lho, S.D. Kim, Nom-uniform steel strip dampers subjected to cyclic loadings, Eng. Struct. 99 (2015) 192–204.
[12] C.H. Lee, S.H. Lho, D.H. Kim, J.T. Oh, Y.K. Ju, Hourglass-shaped strip damper subjected to monotonic and cyclic loadings, Eng. Struct. 119 (2016) 122–134.
[13] B.C. Amadeo, S.H. Oh, H. Akiyama, Ultimate energy absorption capacity of slit-type steel plates subjected to shear deformations, J. Struct. Constr. Eng (Trans. AIJ) 63 (503) (1998) 139–147 (in Japanese).
[14] S.H. Oh, Y.J. Kim, H.S. Ryu, Seismic performance of steel structures with slit dampers, Eng. Struct. 31 (9) (2009) 1997–2008.
[15] Y.J. Kim, T.S. Ahn, J.H. Bae, S.H. Oh, Experimental study of using cantilever type steel plates for passive energy dissipation, Int. J. Steel Struct. 16 (3) (2016) 959–974.
[16] B.K. Hwang, T.S. Kim, Y.J. Kim, J.W. Kim, A comparative study on hysteretic characteristics of austenitic stainless steel and carbon steel slit dampers under cyclic loading, J. Build. Eng. 45 (2022) 103553.
[17] V. Shrinivas, S.K. Varma, L.E. Murr, Deformation-induced martensitic characteristics in 304 and 316 stainless steels during room-temperature rolling, Metall. Mater. Trans. A 26A (1995) 661–671.
[18] Korean Standard (KS), Hot rolled stainless steel plates, sheets and strip, KS D 3705, 2017 (in Korean).
[19] Korean Standard (KS), Rolled steels for general structure, KS D 3503, 2018 (in Korean).
[20] ASTM, ASTM Standard Specification for Stainless Steel Bars and Shapes, ASTM A276/ A276M – 17, ASTM International, 2017.
[21] ASTM, Standard Specification for Carbon Structural Steel, ASTM A36 / A36M – 19, ASTM International, 2016.
[22] Korean Design Standard (KDS), Seismic Building Design Code, KDS 41 17 00, Korea Construction Standards Center, Seoul (in Korea), 2019.
[23] ASCE/SEI 7, Minimum Design Loads for Buildings and Other Structures, American Society of Civil Engineers, Virginia (in USA), 2016.
[24] FEMA461, Interim Testing Protocols for Determining the Seismic Performance Characteristics of Structural and Nonstructural Components, Applied Technology Council, 2007.
[25] Architectural Institute of Korea (AIK), Design Guide and Specification of Vibration Control Structure, Kimoondang, 2010 (in Korean).
[26] Korea Society of Seismic Isolation and Vibration Control, Design Methodology and Application Examples of Vibration Control Structure, Kimoondang, 2015 (in Korean).
[27] Korean Standard (KS), Test pieces for tensile test for metallic materials, KS B 0801, Seoul, Korea, 2007 (in Korean).

[28] Korean Standard (KS), Method of Tensile Test for Metallic Materials, KS B 0802, Seoul, Korea, 2003 (in Korean).
[29] F. Yin, L. Yang, M. Wang, L. Zong, X. Chang, Study on ultra-low cycle fatigue behavior of austenitic stainless steel, Thin-Walled Struct. 143 (2019) 106205.
[30] F. Zhou, L. Li, Experimental study on hysteretic behavior of structural stainless steels under cyclic loading, J. Construct. Steel Res. 122 (2016) 94–109.
[31] ASTM, ASTM Standard Test Method for Strain-Controlled Fatigue Testing, ASTM E606/E606M, ASTM International, 2012.
[32] Korean Standard (KS), Metallic materials - Fatigue testing - Axial-strain-controlled method, KS B ISO 12106, Seoul, Korea, 2004 (in Korean).
[33] S.K. Paul, S. Nicole, H. Timothy, Austenite plasticity mechanisms and their behavior during cyclic loading, Int. J. Fatigue 106 (2018) 185–195.
[34] X. Ma, E. Borchers, A. Pena, H. Krawinkler, S. Billington, G.G. Deierlein, Design and Behavior of Steel Shear Plates with Openings as Energy-Dissipating Fuses, John A. Blume Earthquake Engineering Center Technical Report 173 2010.